



HAL
open science

Acidic Properties of Alkaline-Earth Phosphates Determined by an Experimental-Theoretical Approach

E. Blanco, Q. Gu, J. Couble, L. Martin, T. Onfroy, G. Costentin,
Jean-Francois Paul, Carine Michel, S. Loridant

► **To cite this version:**

E. Blanco, Q. Gu, J. Couble, L. Martin, T. Onfroy, et al.. Acidic Properties of Alkaline-Earth Phosphates Determined by an Experimental-Theoretical Approach. *Journal of Physical Chemistry C*, 2020, 124 (3), pp.2013-2023. 10.1021/acs.jpcc.9b10472 . hal-02472130

HAL Id: hal-02472130

<https://hal.science/hal-02472130v1>

Submitted on 6 Nov 2020

HAL is a multi-disciplinary open access archive for the deposit and dissemination of scientific research documents, whether they are published or not. The documents may come from teaching and research institutions in France or abroad, or from public or private research centers.

L'archive ouverte pluridisciplinaire **HAL**, est destinée au dépôt et à la diffusion de documents scientifiques de niveau recherche, publiés ou non, émanant des établissements d'enseignement et de recherche français ou étrangers, des laboratoires publics ou privés.

This document is confidential and is proprietary to the American Chemical Society and its authors. Do not copy or disclose without written permission. If you have received this item in error, notify the sender and delete all copies.

Acidic Properties of Alkaline-earth Phosphates Determined by an Experimental-Theoretical Approach

Journal:	<i>The Journal of Physical Chemistry</i>
Manuscript ID	jp-2019-10472y.R1
Manuscript Type:	Article
Date Submitted by the Author:	n/a
Complete List of Authors:	Blanco, Elodie; Institut de Recherches sur la Catalyse et l'Environnement de Lyon GU, Qingyi; Ecole normale superieure de Lyon Couble, Julien; Institut de Recherches sur la Catalyse et l'Environnement de Lyon Martin, Lucile; Unité de Catalyse et Chimie du Solide Onfroy, Thomas; UPMC, Laboratoire Systemes Interfaciaux Echelle Nanometrique Costentin, Guylene; UPMC, Lab. Réactivité de Surface Paul, Jean-François; Unité de Catalyse et Chimie du Solide Michel, Carine; Ecole normale superieure de Lyon, Laboratoire de Chimie Loridant, Stephane; Institut de Recherches sur la Catalyse et l'Environnement de Lyon

SCHOLARONE™
Manuscripts

1
2
3
4
5
6
7
8
9
10
11
12
13
14
15
16
17
18
19
20
21
22
23
24
25
26
27
28
29
30
31
32
33
34
35
36
37
38
39
40
41
42
43
44
45
46
47
48
49
50
51
52
53
54
55
56
57
58
59
60

Acidic Properties of Alkaline-earth Phosphates

Determined by an Experimental-Theoretical Approach

Elodie Blanco^a, Qingyi Gu^b, Julien Couble^a, Lucile Martin^c, Thomas Onfroy^d, Guylène Costentin^d, Jean-François Paul^f, Carine Michel^{b,}, Stéphane Loridant^{a,*}*

^a Univ Lyon, Université Claude Bernard-Lyon 1, CNRS, IRCELYON-UMR 5256, 2 av. A. Einstein, F-69626 Villeurbanne Cedex, France

^b Univ Lyon, Ens de Lyon, CNRS UMR 5182, Université Claude Bernard Lyon 1, Laboratoire de Chimie, F69342, Lyon, France

^c Univ. Lille, CNRS, Centrale Lille, ENSCL, Univ. Artois, UMR 8181-UCCS Unité de Catalyse et Chimie du Solide, F-59000 Lille, France

1
2
3
4 ^d Sorbonne Université, CNRS, Laboratoire Réactivité de Surface, LRSUPMC Univ Paris

5
6
7 06, UMR 7197, Laboratoire Réactivité de Surface, F-75005 Paris, France
8
9
10
11
12
13
14
15
16
17
18
19
20
21
22
23
24
25
26
27
28
29
30
31
32
33
34
35
36
37
38
39
40
41
42
43
44
45
46
47
48
49
50
51
52
53
54
55
56
57
58
59
60

1
2
3 **ABSTRACT.** Alkaline-earth phosphates efficient in the dehydration of lactic acid to acrylic
4 acid were previously shown to contain a surface mono/dihydrogen phosphate amorphous
5
6 layer composed by M^{2+} cations, P=O and POH groups. In this work, acidic properties of
7
8 such a layer were determined combining FTIR spectra achieved at the dehydrated state
9
10 and under water vapor and DFT simulations of non-defective and defective MPOH
11
12 structure. The FTIR spectra of adsorbed pyridine and lutidine revealed the presence of
13
14 moderate Lewis acid sites (LAS) and of POH groups interacting by H-bonding without
15
16 significant protonation. DFT calculations were key to interpret FTIR spectra after
17
18 adsorption of NH_3 : when solely adsorbed, NH_3 interacts with the LAS on both the non-
19
20 defective surface and the defective surface while the POH for which H points up towards
21
22 the gas phase are reoriented downward. Brønsted acid sites (BAS) were shown to form
23
24 under water vapor. This phenomenon was shown by DFT to arise from a more acidic
25
26 character of HPO_4^{2-} species for non-defective surface and casual formation of non-
27
28 defective surface leading to higher amount of $H_2PO_4^-$ species, which are more acidic BAS.
29
30
31
32
33
34
35
36
37
38
39
40
41
42
43
44
45
46
47
48
49
50
51
52
53
54
55
56
57
58
59
60

1
2
3
4
5
6
7
8
9
10
11
12
13
14
15
16
17
18
19
20
21
22
23
24
25
26
27
28
29
30
31
32
33
34
35
36
37
38
39
40
41
42
43
44
45
46
47
48
49
50
51
52
53
54
55
56
57
58
59
60

1. INTRODUCTION

Acrylic Acid (AA) is a platform molecule used as a building block to produce acrylate polymers and plastics and currently produced by catalytic oxidation of propylene in large volume (6 Mt/y predicted by 2020).^{1,2} From both environmental and economical point of view, alternative routes to produce acrylic acid should be developed. Glycerol is a potential renewable raw material to produce acrylic acid by oxidehydration.³ Yields higher than 50% were obtained on W-V-Nb mixed oxides with hexagonal tungsten bronze structure.^{4,5}

Another investigated route is the dehydration of Lactic Acid (LA), a platform molecule used to produce chemical commodities and PLA polymers.^{1,2,6} Lactic acid is currently yielded by carbohydrates fermentation^{1,2,6} but can also be obtained by alternative fermentation processes using various substrates^{7,8} and by glycerol catalytic dehydrogenation.⁹ The global market for lactic acid was 0.75 Mt/y in 2017 and is projected to reach 1.8 Mt/y by 2022.¹⁰ Modified zeolites, sulphates/nitrates, and phosphates were specifically investigated. The best yields were obtained using alkaline earth metal phosphates (up to 85% AA yield) which furthermore are more stable than zeolites.^{1,2,6}

We established correlations between the NH₃ and CO₂-TPD curves and the AA selectivity using alkaline earth phosphates as catalysts.¹¹ The catalysts with only weak acid and basic sites were selective and their NH₃ and CO₂-TPD curves were surprisingly quite similar. Furthermore, the best AA selectivity was obtained for barium orthophosphate, for which the acid to base balance was close to 1. It suggested the participation of acid-base pairs in the mechanism. However, TPD measurements were achieved after pre-treatment at the calcination temperature while water vapor was present in the reaction feed and generated by dehydration. More recently, characterization of the prepared alkaline earth phosphates (including barium orthophosphate) showed the systematic

1
2
3 presence of a surface mono/dihydrogen phosphate amorphous (non-crystalline for X-rays and
4 electron diffraction) layer containing POH species.¹² *In situ* DRIFT measurements have suggested
5 that formation of POH groups was favored under water vapor and that these species interacted
6 with reactants or reaction products at the reaction temperature.
7
8
9
10

11
12 DFT calculations could help in rationalizing the experimental observations. For instance,
13 Paul and co-workers investigated the LA to AA transformation but on ZrO₂.¹³ They identified that
14 on this oxide, the dehydration site is clearly an acido-basic pair, where the acid site Zr⁴⁺ stabilizes
15 the leaving α -OH and the basic O²⁻ site on zirconia plays the role of proton acceptor. Theoretical
16 studies were also achieved on alkaline earth phosphates but mostly on hydroxyapatites
17 Ca₅(PO₄)₃(OH) due to their important using in biomaterials.¹⁴
18
19
20
21
22
23
24
25

26 In the present work, acidic sites of alkaline-earth phosphates catalysts were characterized
27 by NH₃ adsorption followed by IR spectroscopy at the dehydrated state and in the presence of
28 water vapor. The IR spectra were assigned from DFT calculations, which also explained acidic
29 properties determined by NH₃ adsorption. Characterization of acidity was strengthened by
30 adsorption of pyridine and lutidine followed by IR spectroscopy.
31
32
33
34
35
36
37
38
39

40 2. METHODS

41 2.1 Catalysts preparation

42 Barium orthophosphate (labelled BaOP) was prepared by mixing a solution of diammonium
43 hydrogen phosphate (NH₄)₂HPO₄ (Aldrich, 99%) at 0.20 mol.L⁻¹ for which the pH was previously
44 adjusted to 9 adding NH₄OH (32%vol) and a solution of barium nitrate (Ba(NO₃)₂) (Aldrich,
45 >99%) at 0.30 mol.L⁻¹. The latter one was added drop wise while maintaining constant the pH and
46 stirring for 1 h. The precipitate was filtrated off, washed with deionized water, dried at 100 °C and
47
48
49
50
51
52
53
54
55
56
57
58
59
60

1
2
3 crushed before calcination under air flow at 600 °C for 6 h.
4
5

6 7 8 **2.2 Catalysts characterizations** 9

10 Analysis of the acidic properties of samples was performed by adsorption-desorption of
11 pyridine and lutidine followed by infrared spectroscopy. Self-supported wafers were placed inside
12 the IR cell and then outgassed under secondary vacuum at 350 °C for 2 h. In the following, the
13 samples were contacted at room temperature with gaseous basic probe via a separate cell
14 containing liquid pyridine or lutidine. The spectra were then recorded following desorption at
15 increasing temperature with a Bruker Vector 22 spectrometer (resolution 2 cm⁻¹, 64 scans). The
16 reported spectra were obtained after subtraction of the spectrum recorded before probe adsorption.
17
18

19 *In situ* DRIFT spectra were achieved with a Nicolet 6700 FTIR spectrometer (Thermo
20 Scientific) equipped with Praying Mantis™ High Temperature Reaction Chamber (Harrick, model
21 HVC-DRP-4). The CaF₂ windows used for the experiments were heated at 70-80 °C with external
22 water system to avoid condensation. The effect of water was investigated by flowing 30%H₂O-He
23 or 30%D₂O-He at 380 °C after pre-treatment at 380 °C for 30 min under He. Such high water
24 partial pressure was obtained using a saturator heated at 70 °C. The background corresponded to
25 the spectrum of dehydrated KBr.
26
27

28 *In situ* FTIR acidity measurements were performed on self-supported pellets (53 mg) with a
29 Nicolet 6700 spectrometer (ThermoScientific) using a homemade stainless steel IR cell reactor
30 specially designed to limit the gas phase contribution (its optical path is 2.2 mm)¹⁵ and NH₃ as
31 probe molecule. This IR cell allowed the study of adsorbed species in the range 20-450 °C under
32 gas flow rates (200 mL.min⁻¹ in the present study) of gas mixtures at atmospheric pressure such as
33 x% NH₃/y% H₂O/He with x and y in the ranges 0-1% and 0-3% respectively. The amount of H₂O
34
35
36
37
38
39
40
41
42
43
44
45
46
47
48
49
50
51
52
53
54
55
56
57
58
59
60

1
2
3 was controlled using a saturator/condenser system as described previously.¹⁶ BaOP pellet was pre-
4 treated at 380 °C under 20%O₂-He for 1 h and then He. NH₃ adsorption equilibrium was followed
5 at 2%NH₃ upon heating and cooling between RT to 200 °C. The AEIR (Adsorption Equilibrium
6 InfraRed spectroscopy) method was used to determine individual NH₃ heats of adsorption from
7 the evolution of the IR band area of each adsorbed X_{ads} species with the increase in T_a in isobaric
8 conditions. The experimental curve $\theta X_{\text{exp}} = f(T_a)$, with θ corresponding to the coverage of sites,
9 was compared to the one obtained from the Temkin model assuming localized adsorbed species.
10 Adjustment of the theoretical curve to the experimental data provides E_x(1) and E_x(0), the heats of
11 adsorption at high and low coverages of the X_{ads} species, respectively. The accuracy of the method
12 to determine NH₃ heats of adsorption has been evidenced for TiO₂ support and V₂O₅/WO₃/TiO₂
13 catalysts.¹⁷⁻¹⁹ Acidity measurements in presence of water vapor²⁰ were achieved at adsorption
14 equilibrium flowing 1%NH₃-3%H₂O-He mixture upon heating and cooling between RT and 200
15 °C.
16
17
18
19
20
21
22
23
24
25
26
27
28
29
30
31
32
33
34

35 **2.3 DFT Computational details**

36
37 Density functional theory (DFT) calculations were carried out using the Vienna ab initio
38 simulation package (VASP).²¹⁻²³ The exchange and correlation terms were obtained by the
39 Perdew–Burke–Ernzerhof form of Generalized Gradient Approximation (GGA-PBE) functional.²⁴
40 The core electrons were kept frozen and a projector-augmented wave (PAW) method was used to
41 substitute the core electrons.²⁵ A cut-off energy of 550 eV of the plane wave basis set was used to
42 describe the valence electrons. The bulk optimization would reach the convergence when the
43 energy was converged to 1×10⁻⁶ eV and the forces were smaller than 0.01 eV/Å with a k-point
44 mesh of 5×2×5. For optimization of the slab, the same energy convergence criterion was used and
45
46
47
48
49
50
51
52
53
54
55
56
57
58
59
60

1
2
3 the convergence criterium on the forces was set to 0.03 eV/Å. The k-point mesh was adapted to
4
5 the super cell size using a mesh of 5×5×1 k-points. Frequencies were computed within the
6
7 harmonic approximation. Gibbs free energies were derived using those frequencies, and for the
8
9 molecules using the perfect gas and rigid rotator approximations.
10

11
12 Based on the previous characterizations of the BaOP catalyst^{11,12} and on the fact that Ca and
13
14 Ba are expected to have similar properties being both alkaline-earth elements, we selected the
15
16 Brushite, a well-known layered calcium hydrogen orthophosphate dihydrate,²⁶⁻²⁸ to model the
17
18 amorphous layer lying over the catalyst crystallites. In solution, Brushite forms thin hexagonal
19
20 platelet.^{27,29} Since the (010) surface corresponds to the basal plane of the platelets, it is expected
21
22 to be the most stable and have a very low surface energy. In order to define a model of this surface,
23
24 the cutting plane was located in the middle of the gap between two layers. The number of water
25
26 molecule was kept equal to the number in the solid. Using this choice, the surface is created cutting
27
28 only hydrogen bonds. Two other planes perpendicular to the basal plane were studied: the (100)
29
30 and the (001) in order to model the edges of the platelets. The two surfaces have been defined
31
32 without breaking any P-O or O-H bonds, in order to reduce their surface energies. For the three
33
34 surfaces, symmetric and stoichiometric slabs were used with a vacuum layer of 15.14 Å to avoid
35
36 the interaction between the slabs. The computed surface energies for (001), (010) and (100) were
37
38 0.047 eV/Å², 0.016 eV/Å² and 0.032 eV/Å² respectively, confirming the greater stability of the
39
40 (010) surface.
41
42
43
44
45

46
47 The adsorption of the molecules was performed on the top of the most favorable surface (010)
48
49 surface using a p(2×2) asymmetric slab made of 16 CaHPO₄·2H₂O, where the top surface layers,
50
51 including 8 CaHPO₄·2H₂O, were allowed to relax while the bottom 8 CaHPO₄·2H₂O were
52
53 constrained during the geometry optimization.
54
55
56
57
58
59
60

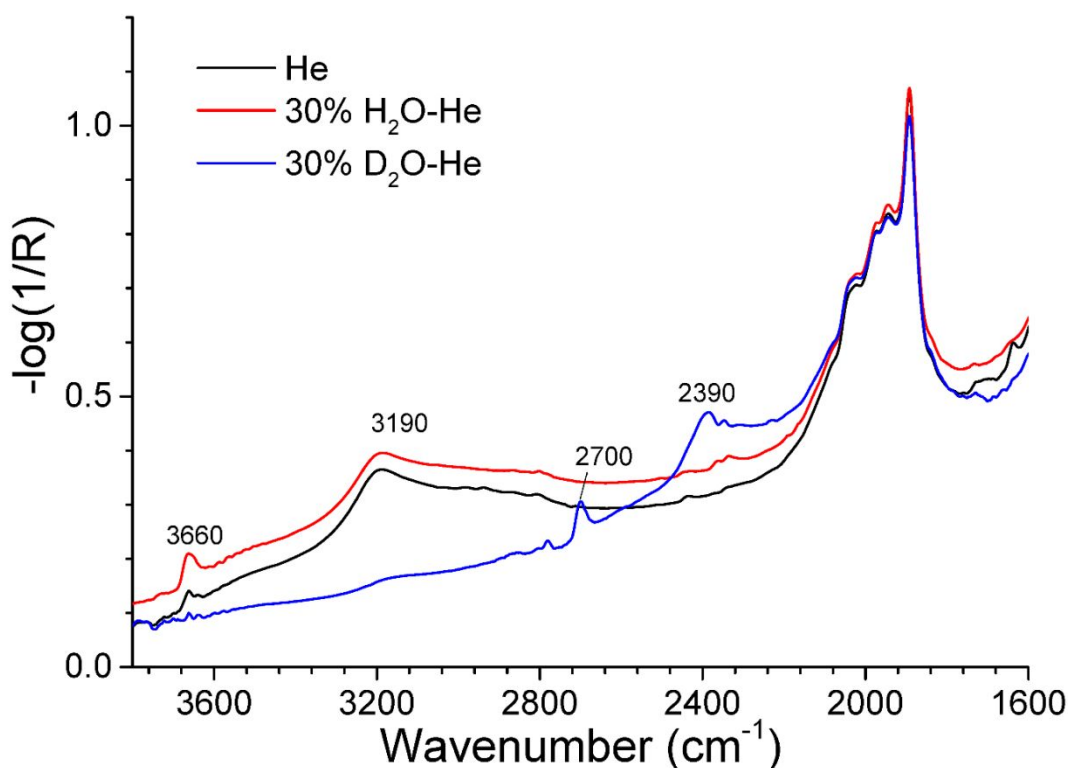
1
2
3 The IR spectroscopy was modelled by accurately determining the vibrational spectrum of a
4 system. We used the density functional perturbation theory in our study to determine the Hessian
5 matrix, and finally obtain the wavenumber of every vibration mode.³⁰ Within this framework, the
6 overtones are not simulated and the influence of the temperature on the vibration wavenumbers is
7 not included. We determined the scaling factor between experimental wavenumbers and DFT ones
8 using NH₃ and H₂O as a reference and we obtained 0.98 for the stretching vibration modes and
9 1.00 the for bending ones as shown in Table S1 of Supplementary material. Scaling down some
10 wavenumbers to improve the quality of the prediction obtained within the harmonic approximation
11 allows us to partially recover anharmonicity effects.³¹⁻³³ The good agreement with the
12 experimental spectra confirms that this factor established on gas phase spectra of water and
13 ammonia is still valid for adsorbed species.
14
15
16
17
18
19
20
21
22
23
24
25
26
27
28
29
30

31. RESULTS

32. 3.1 Characterization of the dehydrated and hydrated state

33 The main structural and textural properties of BaOP catalyst have been previously described.¹¹
34 Shortly, it contained mostly crystalline Ba₃(PO₄)₂ and its specific surface area was 8.9 m².g⁻¹.
35 Chemical and XPS analyses showed sub-stoichiometric Ba/P ratios (1.38 and 1.28, respectively
36 instead of 1.5 for stoichiometric Ba₃(PO₄)₂) that could be ascribed to the presence of either small
37 amount of crystalline α-Ba₂P₂O₇¹¹ and a phosphorus rich amorphous (non-crystalline) phase
38 which does not diffract either by X-rays and electron diffractions. The latter phase was shown to
39 correspond to a surface layer containing POH species and lying over Ba₃(PO₄)₂ crystallites.¹² It
40 could be either a stoichiometric BaHPO₄ or a mixture of mono and dihydrogen phosphate with a
41 general formula Ba_(1-x)(HPO₄)_{1-2x}(H₂PO₄)_{2x}.
42
43
44
45
46
47
48
49
50
51
52
53
54
55
56
57
58
59
60

1
2
3 A DRIFT spectrum of BaOP treated under helium flow at 380 °C is plotted in Figure 1. The
4
5 bands between 1850 and 2050 cm^{-1} corresponded to overtones of $\nu(\text{P}=\text{O})$ vibrations which are
6
7 located around 1000 cm^{-1} .³⁴ The band at 3660 cm^{-1} was ascribed to $\nu(\text{PO-H})$ stretching vibrations
8
9 of free surface species by analogy with deficient hydroxyapatites.¹² The broad band located around
10
11 3190 cm^{-1} corresponded to $\nu(\text{PO-H})$ stretching vibrations as observed for alkaline earth hydrogen
12
13 phosphates.³⁵⁻³⁸ This large difference of wavenumber could arise from the effect of hydrogen
14
15 bonds in bulk hydrogen phosphates leading to weakening of PO-H bonds and stretching vibrations
16
17 at lower wavenumbers.
18
19
20
21



47
48 **Figure 1.** *In situ* DRIFT spectra of BaOP at 380 °C under He, 30% H_2O -He and 30% D_2O -He. The background
49 corresponds to the spectrum of dehydrated KBr (the R reflectance is equal to I/I_{KBr}).
50
51

52
53
54 The DRIFT spectrum recorded under 30% H_2O -He flow at the same temperature was similar.
55
56
57
58
59
60

1
2
3 However, the absorbance of the $\nu(\text{PO-H})$ band at 3660 cm^{-1} was increased evidencing formation
4
5 of additional POH species. This phenomenon could arise from hydrolysis of the weak amount of
6
7 $\alpha\text{-Ba}_2\text{P}_2\text{O}_7$ leading to BaHPO_4 . Note that the δ bending mode of chemisorbed H_2O at $1600\text{-}1630$
8
9 cm^{-1} ^{39,40} was not observed showing such species was not present at the surface of BaOP sample.
10
11 Isotopic labelling achieved under $30\%\text{D}_2\text{O-He}$ at $380\text{ }^\circ\text{C}$ led to a shift of the bands at 3660 and
12
13 3190 cm^{-1} to 2700 and 2390 cm^{-1} , respectively while the framework vibrational bands at 1850-
14
15 2050 cm^{-1} remained unchanged. These shifts are close to the ones expected for deuteration of OH
16
17 groups considering harmonic oscillator (ratios of 0.74 and 0.75 , respectively instead of 0.73).
18
19
20
21
22
23

24 3.2 Modelling of the surfaces and influence of the water amount

25
26 The Brushite structure was built based on the neutron single crystal diffraction study²⁶ with a
27
28 composition of $4\text{ CaHPO}_4\cdot 2\text{H}_2\text{O}$ and a C-centered monoclinic cell within the space group Cc
29
30 ($\#9, C_s^4$), as shown in Figure 2.
31
32

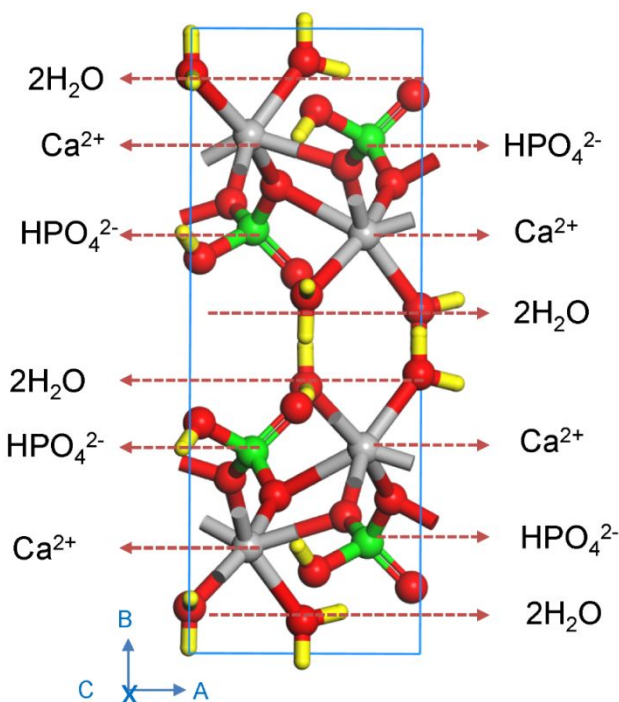
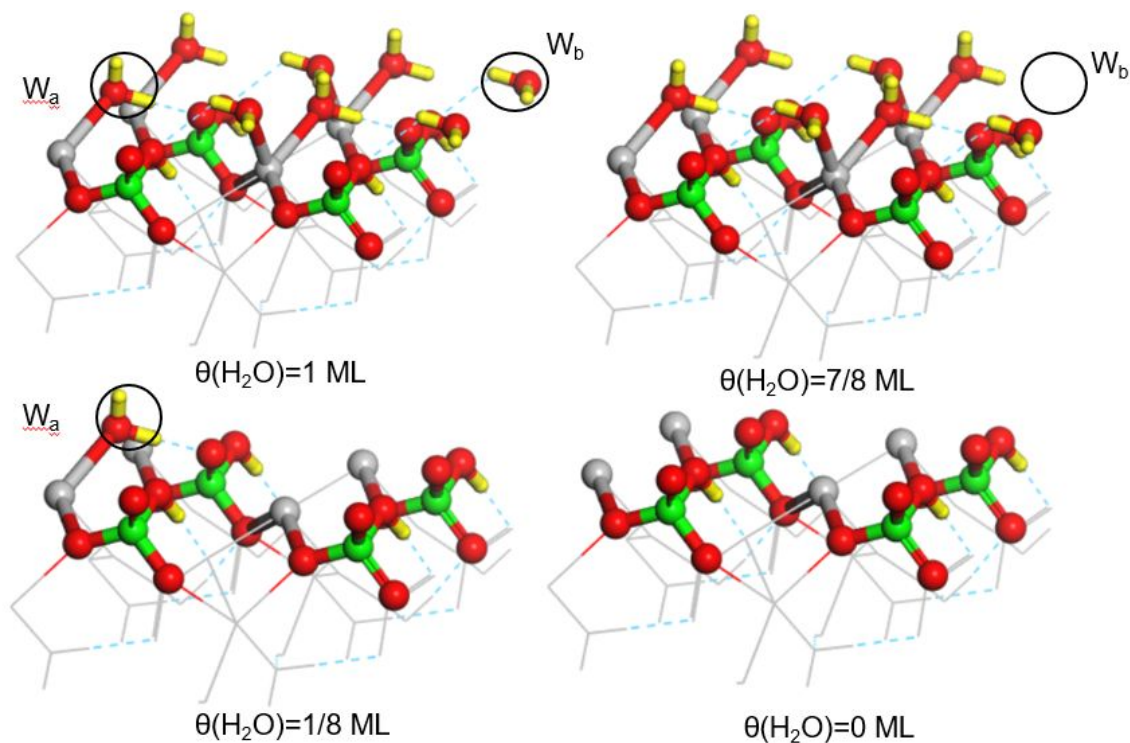


Figure 2. Unit cell of the layered structure of the Brushite, containing Ca atoms (grey), O atoms (red), H atoms (yellow) and P atoms (green).

The calculated cell parameters of $a = 5.98 \text{ \AA}$, $b = 15.14 \text{ \AA}$ and $c = 6.24 \text{ \AA}$, are in good agreement with the experimental ones ($a_{\text{exp}} = 5.80 \text{ \AA}$, $b_{\text{exp}} = 15.13 \text{ \AA}$, $c_{\text{exp}} = 6.32 \text{ \AA}$).²⁶ A detailed description of the brushite structure can be found in the Hirsch's work.²⁷

The (010) surface of Brushite is the most stable surface computed (see computational details). As shown in Figure 3, the top of this surface is covered with eight water molecules per unit cell. We will consider later this as a complete monolayer of water, $\theta(\text{H}_2\text{O})=1 \text{ ML}$. One can distinguish two orientations: (i) water marked W_a is perpendicular to the surface, 2.55 \AA far away from the nearest Ca^{2+} atom, and gives a H bond to the O of HPO_4^{2-} and accepts an H bond from another water molecule nearby (ii) the other water, W_b , is parallel to the surface, closer to Ca^{2+} with a distance of 2.47 \AA and is also involved in a H bond network, donating to HPO_4^{2-} and to W_a .



1
2
3 **Figure 3.** Structures of the (010) surface of $\text{CaHPO}_4 \cdot n\text{H}_2\text{O}$ with different water coverages, $\theta(\text{H}_2\text{O})=1$ ML, $7/8$
4 ML, $1/8$ ML and 0 ML. Only half of the surface structure is shown here for simplicity. The two different types of
5 water molecules are marked as W_a and W_b , highlighted by a black circle in the top left structure, which corresponds to
6 the structure obtained as cleaved from the bulk. The H bond network of W_a and W_b is shown in light blue dashed lines.
7
8
9
10
11 At 1ML, 8 water molecules are found. At $7/8\text{ML}$, one W_b water has been removed and the black circle indicates its
12 former position. At $1/8\text{ML}$, only one water molecule remains (W_a type) as highlighted by a black circle. Color-coding:
13
14 grey for calcium, red for oxygen, green for phosphorus and yellow for hydrogen.
15
16
17

18
19 This highly hydrated surface can be easily dehydrated raising the temperature. The fully
20 hydrated surface as cleaved from the bulk structure has a water coverage of $\theta(\text{H}_2\text{O})=1$ ML, which
21 corresponds to eight water molecules per unit cell. We considered various coverages in water,
22
23 $\theta(\text{H}_2\text{O})=1$ ML, $7/8$ ML, $1/8$ ML and 0 ML, as shown in Figure 3. To start, we generated a structure
24
25 with a lower coverage of $\theta(\text{H}_2\text{O})=7/8$ ML removing one water molecule. The structure with W_b
26
27 deleted is $-20 \text{ kJ} \cdot \text{mol}^{-1}$ more stable than the one where W_a is deleted, thus only the surface with W_b
28
29 deleted is shown in Figure 3. Next, we built a weakly hydrated surface, keeping only one water
30
31 (W_a), reaching a coverage of $\theta(\text{H}_2\text{O})=1/8$ ML. Finally, a fully dehydrated surface was also
32
33 computed ($\theta(\text{H}_2\text{O})=0$ ML), where the eight water molecules exposed at the external surface were
34
35 deleted but the ones inside and in the bottom layers were still preserved. The relative stability of
36
37 these surfaces as function of the temperature under 1 atm pressure of water is shown in Figure 4.
38
39
40
41
42
43
44
45
46
47
48
49
50
51
52
53
54
55
56
57
58
59
60

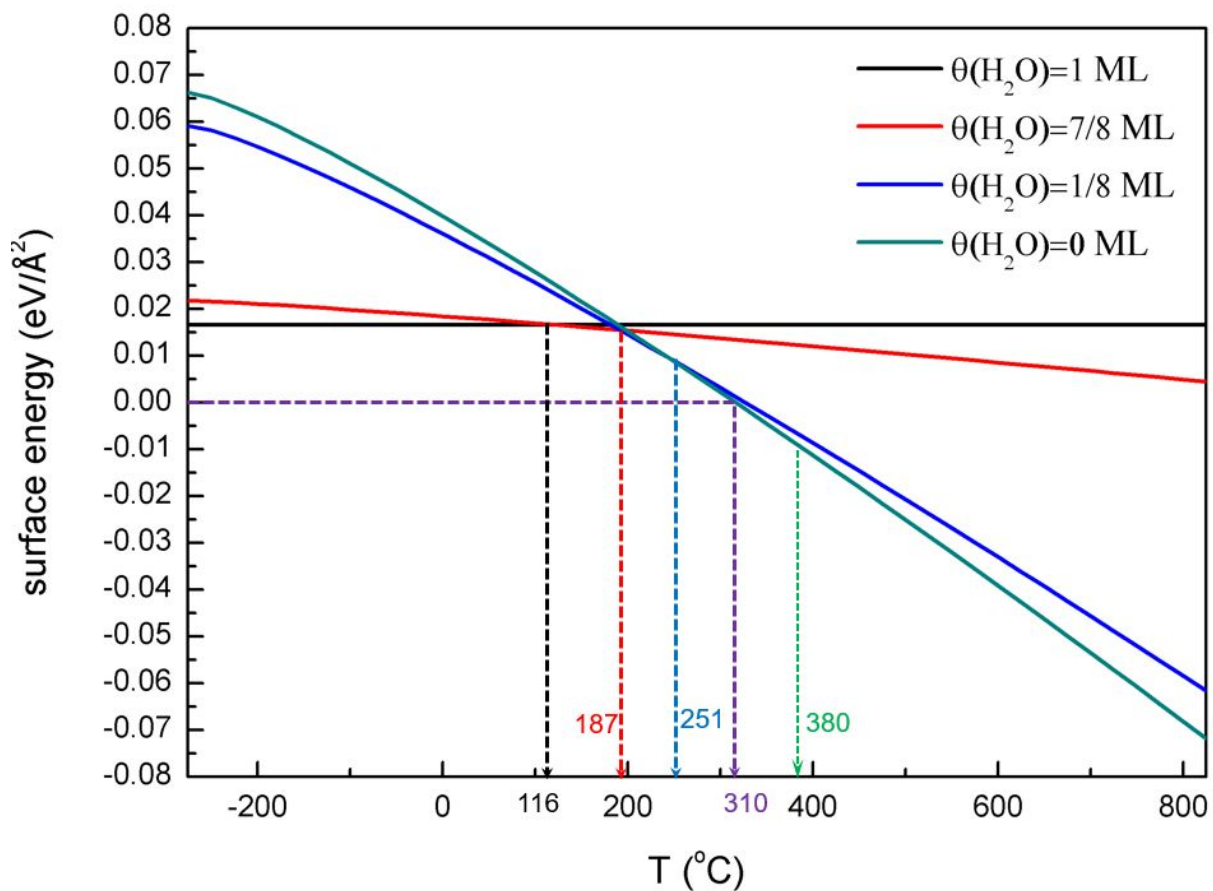


Figure 4. Surface energy in $\text{eV}/\text{\AA}^2$ of Brushite (010) surfaces with various coverages ($\theta(\text{H}_2\text{O})=1 \text{ ML}$, $7/8 \text{ ML}$, $1/8 \text{ ML}$ and 0 ML) in water as function of the temperature and under a pressure in water of 1 atm.

When the temperature is lower than $116 \text{ }^\circ\text{C}$, the surface prefers to be covered with water. At $116 \text{ }^\circ\text{C}$, the surface starts to dehydrate, one W_b is desorbed and the exposed surface has a coverage of $\theta(\text{H}_2\text{O})=7/8 \text{ ML}$. This temperature threshold for dehydration is consistent with the experimental one ($80 \text{ }^\circ\text{C}$) found by Dosen et al.⁴¹ With an increase in the temperature, the dehydration keeps proceeding and at $187 \text{ }^\circ\text{C}$, a coverage of $\theta(\text{H}_2\text{O})=1/8 \text{ ML}$ is reached and when the temperature is higher than $251 \text{ }^\circ\text{C}$, the surface is totally dehydrated. It should also be noted that the surface energy becomes negative when the temperature is higher than $310 \text{ }^\circ\text{C}$, which means that a dehydration of the bulk should occur. Such transformation to CaHPO_4 (Monetite)¹⁴ was not further investigated

1
2
3 since the purpose was to build a model of the exposed facet of the BaOP catalyst. However, these
4
5 temperatures of complete dehydration of the surface and of likely bulk dehydration are consistent
6
7 with experimental observations where the transformation to Monetite is complete between 200
8
9 and 220 °C.⁴¹ Based on the above discussion, it is clear that at the reaction temperature of 380 °C
10
11 (which is also the IR spectrum recording temperature), the most favorable surface is the dehydrated
12
13 surface. For experiments performed under 30% H_2O -He, we will include one water molecule to
14
15 probe the impact of the modifications induced by the change of atmosphere and consider the
16
17 $\theta(\text{H}_2\text{O})=1/8\text{ML}$ coverage.
18
19

20
21 As the amorphous layer lying over $\text{Ba}_3(\text{PO}_4)_2$ crystallites of the BaOP catalyst could be a phase
22
23 with a general formula $\text{Ba}_{(1-x)}(\text{HPO}_4)_{1-2x}(\text{H}_2\text{PO}_4)_{2x}$ (see above), a defective surface was also
24
25 constructed with a cationic vacancy and completed with two H^+ . The most favorable structure of
26
27 this defective surface is shown in Figure 5. The two additional H^+ are added on two HPO_4^{2-}
28
29 yielding two H_2PO_4^- groups. One of the additional H points down, forming an H bond with another
30
31 HPO_4^{2-} deeper in the surface. This orientation is labeled H_{down} . The other additional H points up
32
33 towards the gas phase and is labeled H_{up} . No other stable configuration can be found with the two
34
35 additional H^+ pointing downward. The adsorption of water is not stronger on this Ca^{2+} vacancy
36
37 than on the non- defective surface (adsorption energy of $-84 \text{ kJ}\cdot\text{mol}^{-1}$ vs. $-82 \text{ kJ}\cdot\text{mol}^{-1}$ respectively).
38
39
40
41
42
43
44
45
46
47
48
49
50
51
52
53
54
55
56
57
58
59
60

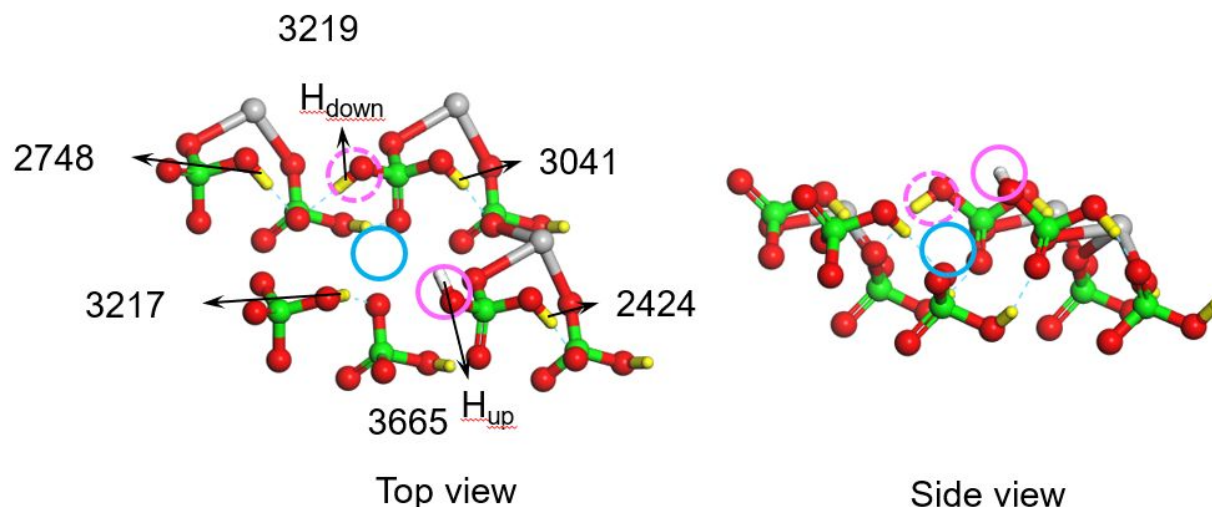
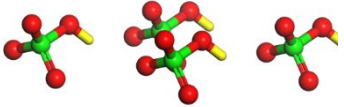
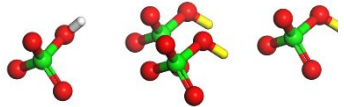
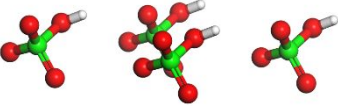


Figure 5. Computed structure of the defective surface. The Ca^{2+} vacancy is shown with a blue circle, the H_{down} with a pink dashed circle and H_{up} with a pink solid circle. The calculated wavenumbers (after rescaling as mentioned in the 2.3 section) of $\nu(\text{PO-H})$ vibrations on the first layer are also shown nearby in cm^{-1} . Color-coding: grey for calcium, red for oxygen, green for phosphorus and yellow for hydrogen, except surface H_{up} which is marked in white.

To determine if the presence of the H_{up} pointing toward the gas phase appears as typical of the presence of a Ca^{2+} vacancy, we also investigated the likeliness of finding such an orientation in the non-defective fully dehydrated surface. The corresponding results are collected in Table 1. The most stable structure is Config 1, with four H_{down} , already discussed and shown in Figure 3. With one H_{up} , Config 2 is only $11 \text{ kJ}\cdot\text{mol}^{-1}$ higher in energy, which corresponds to a Boltzmann probability of 0.15 at the working temperature of $380 \text{ }^\circ\text{C}$. However, with four H_{up} , Config 3 is much less stable and is clearly very unlikely at this temperature. In other words, the presence of H_{up} cannot be attributed only to the presence of Ca^{2+} vacancy but is also related to thermal effects that favor the re-orientation of the PO-H bond.

Table 1. Influence of the PO-H orientation in the non-defective dehydrated (010) surface of Brushite on the stability at 380 °C and the computed wavenumbers of $\nu(\text{PO-H})$, reported after rescaling as mentioned in the 2.3 section.

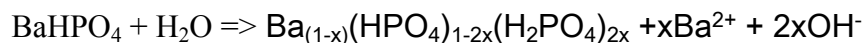
No.	Surface structure*	Relative energy /kJ.mol ⁻¹	Boltzmann distribution	$\nu(\text{PO-H}_{\text{up}})$ /cm ⁻¹	$\nu(\text{PO-H}_{\text{down}})$ /cm ⁻¹
Config 1		0	0.84	\	3170, 3161
Config 2		11	0.15	3691	3200-3133
Config 3		47	0.0002	3692	\

* H_{up} shown in white and H_{down} shown in yellow.

These two orientations (up and down) have a clear spectroscopic signature, with distinct $\nu(\text{PO-H})$ stretching vibrations. In the non-defective dehydrated surface, the free PO-H_{up} is found to vibrate around 3690 cm^{-1} while the $\text{PO-H}_{\text{down}}$ vibrations are red-shifted to the 3100-3200 cm^{-1} range due to their involvement in strong H-bonds with internal HPO_4^{2-} as shown in Table 1. In a defective surface, the vibration of free PO-H_{up} is around 3660 cm^{-1} and two vibrations of $\text{PO-H}_{\text{down}}$ are around 3220 cm^{-1} (Figure 5). These two computed wavenumbers are in agreement with the observations reported in Figure 1 with two bands at 3660 and 3190 cm^{-1} identified as P-OH vibrations. However, in the defective surface, several $\nu(\text{PO-H}_{\text{down}})$ wavenumbers are much lower (3041 cm^{-1} , 2748 cm^{-1} and 2424 cm^{-1}) due to the change of the environment induced by the deletion of one Ca^{2+} atom and the addition of two more protons on the HPO_4^{2-} groups leading to H_2PO_4^- . They could explain the large width of the band at 3190 cm^{-1} (see Figure 1) tailing to 2400 cm^{-1} .

1
2
3 This would imply that the surface of the BaOP catalyst was a defective hydrogen phosphate and
4 hence contained H_2PO_4^- species.
5
6

7
8 To further confirm the interpretation of the *in situ* DRIFT spectra of BaOP at 380 °C under
9 He but also under 30% H_2O -He and 30% D_2O -He (Figure 1), we also considered the case with 1/8
10 ML of water (see Figure 4 and the corresponding discussion). The increase of the band at 3660
11 cm^{-1} in presence of water cannot be attributed to water itself since the δ bending mode of
12 chemisorbed H_2O at 1600-1630 cm^{-1} ^{39,40} was not observed. However, all attempts to increase the
13 amount of P-OH exposed thanks to water dissociation failed, on both the non-defective dehydrated
14 and the defective surfaces. The only stable structure was obtained in the case of the non-defective
15 surface (as shown in Figure S1) but it is 167 $\text{kJ}\cdot\text{mol}^{-1}$ less stable than when water is not dissociated.
16 Since the increase of the band at 3660 cm^{-1} cannot be attributed to water itself or to the increase of
17 the number of POH by water dissociation, we checked if the stability of the P-OH_{up} could be
18 increased by the presence of a chemisorbed water molecule: as shown in Table S2, turning one P-
19 OH_{down} into a P-OH_{up} costs 9 $\text{kJ}\cdot\text{mol}^{-1}$, which is very close to the 11 $\text{kJ}\cdot\text{mol}^{-1}$ that was needed in
20 absence of water (Table 1): the effect is not significant. Finally, we inferred that it could be related
21 to hydrolysis of the small amount of $\alpha\text{-Ba}_2\text{P}_2\text{O}_7$ present in the BaOP catalyst leading to BaHPO_4
22 formation and to an increase in the concentration of cationic vacancy in the hydrogen phosphate
23 layer lying over $\text{Ba}_3(\text{PO}_4)_2$ crystallites, which would be favored by water. For BaHPO_4 , the
24 hydrolysis reaction is proposed to occur according to:
25
26
27
28
29
30
31
32
33
34
35
36
37
38
39
40
41
42
43
44
45
46



47
48 Note that similar dissolution processes were reported in the liquid phase^{42,43} and could be more
49 favorable for sub-stoichiometric brushite containing cationic vacancies.
50
51
52
53
54
55
56
57
58
59
60

3.3 Acidity measurements by IR spectroscopy

The FTIR spectrum of pyridine adsorbed on BaOP plotted in Figure S2 (supplementary material) contained bands at 1614, 1592, 1574, 1489 and 1441 cm^{-1} which were attributed to pyridine coordinated to Lewis acid sites (LAS) or in H-bonding.^{44,45} Observation of two 8a vibrational modes at 1614 and 1592 cm^{-1} revealed the presence of two different coordination sites. Considering their shifts compared to pyridine in liquid phase (1583 cm^{-1}), they were attributed to moderate Lewis acid and H-bonding sites, respectively. The three other bands corresponded to 8b, 19a and 19b modes, respectively.^{44,45} The absence of band around 1540-1550 cm^{-1} typical of pyridinium cations indicated the absence of Brønsted acid sites able to protonate pyridine.

As pyridine ($\text{pK}_a=5.2$) could be too weak to react with BAS, adsorption-desorption of lutidine ($\text{pK}_a=6.6$) was followed by FTIR. Spectra recorded at different desorption temperatures are plotted in Figure 6.

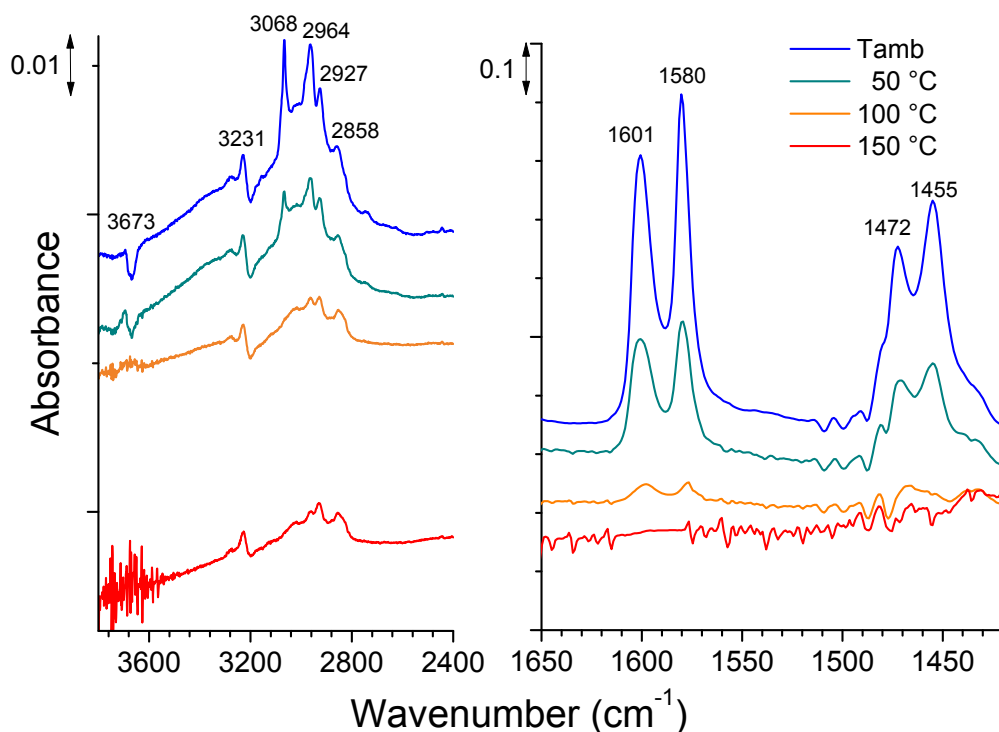


Figure 6. Evolution of the FTIR spectra of BaOP after adsorption of lutidine at T_{amb} and desorption under vacuum at increasing temperature.

1
2
3 At room temperature, bands were observed at 1601, 1580, 1472 and 1455 cm^{-1} which were
4 attributed to the 8a, 8b, 19a and 19b vibrational modes of lutidine coordinated to LAS or in H-
5 bonding^{46,47} while the negative $\nu(\text{PO-H})$ band at 3673 cm^{-1} revealed structural modifications of
6 POH_{up} species that could arise from interaction between POH_{up} species and lutidine. It was not
7 possible to know if the broad band around 3200 cm^{-1} and attributed to POH_{down} was affected
8 because of superimposition of $\nu(\text{CH}_3)$ and $\nu(\text{CH})$ stretching vibrations of lutidine. The 8a mode of
9 lutidine is very sensitive to the adsorption mode and its small shift compared to the liquid phase
10 (+7 cm^{-1}) was typical of H-bonded species. The 8a mode of lutidinium cations located at 1640-
11 1655 cm^{-1} was not observed showing that POH species were not able to protonate lutidine.
12 Increasing the desorption temperature, the bands of H-bonded lutidine disappeared in parallel to
13 the negative $\nu(\text{PO-H})$ band confirming their interdependence. The steric hindrance of methyl
14 groups of lutidine could explain such molecule did not probe moderated LAS contrarily to
15 pyridine.⁴⁷

16
17
18
19
20
21
22
23
24
25
26
27
28
29
30
31
32
33 The *in situ* FTIR spectra recorded at adsorption equilibrium of NH_3 are shown on Figure 7
34 from 120 to 7 $^{\circ}\text{C}$. They all contain one band at 1630 cm^{-1} , numerous bands between 3200 and 3400
35 cm^{-1} and a negative band at 3670 cm^{-1} . They disappeared above 200 $^{\circ}\text{C}$ in good agreement with
36 TPD measurements. Comparison between the evolutions of the experimental coverage and the one
37 calculated using the Temkin model (Figure S3) led to adsorption heat values of $E_0 = 65 \text{ kJ}\cdot\text{mol}^{-1}$
38 and $E_1 = 48 \text{ kJ}\cdot\text{mol}^{-1}$. Such low values were typical of weak adsorption sites.¹⁷

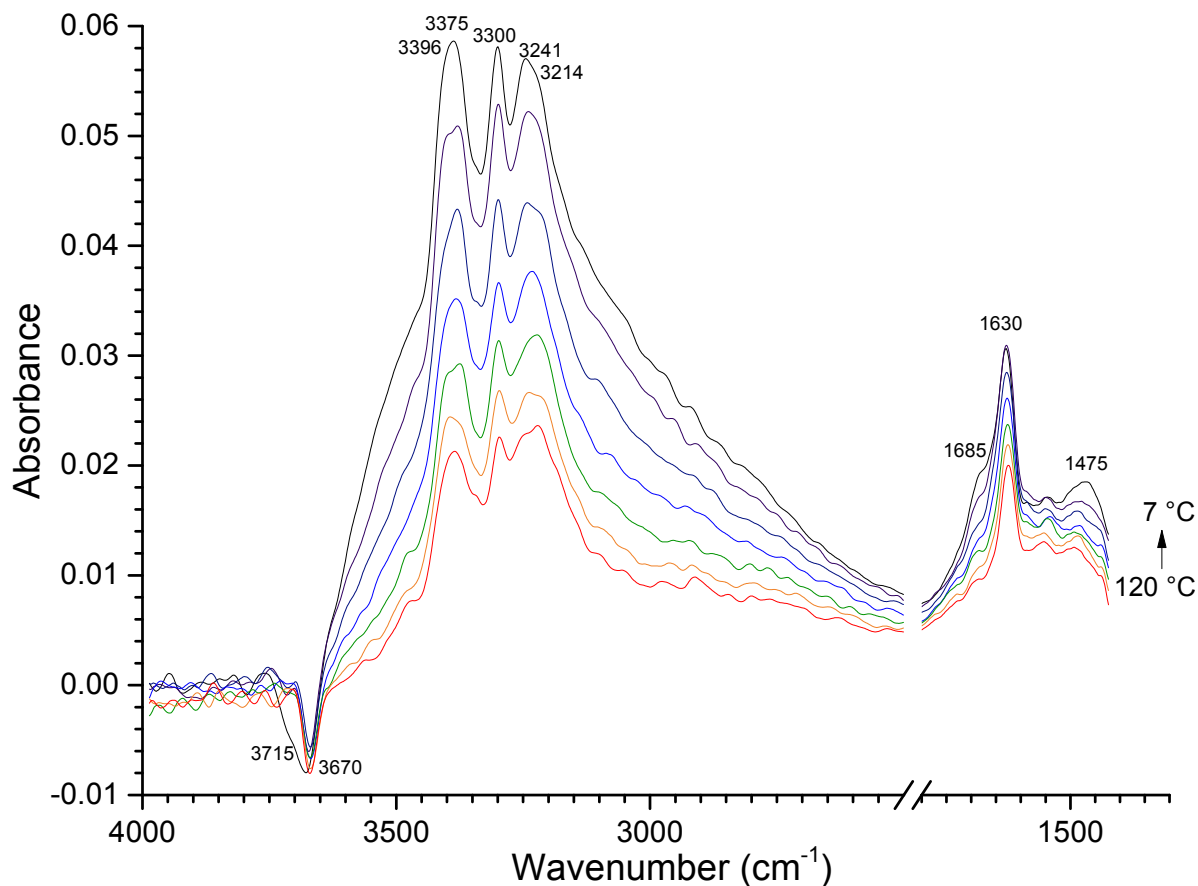


Figure 7. Evolution of the IR bands of NH₃ adsorbed species on pre-treated BaOP catalyst recorded under 2%NH₃-He flow from 120 to 7 °C. The backgrounds correspond to the spectra recorded after pretreatment under He flow at the same temperatures, mass of the pellet 53 mg.

We also established the relative stability of various ammonia surface concentrations as function of the temperature using ab initio thermochemistry (see Figure S4). When $T < 145$ °C, the coverage of NH₃ was $\theta(\text{NH}_3)=1$ ML (one ammonia per surface phosphate). It decreased to 1/2 ML from 145 °C to 162 °C. Above 162 °C, the surface was predicted to be bare, with no ammonia, in agreement with our experimental observations. To sustain the attribution of the bands and identify the corresponding sites, we show the most important predicted wavenumbers obtained on the dehydrated surfaces with a coverage of $\theta(\text{NH}_3)=1/4$ ML in Figure 8. The ones obtained with a

higher coverage, such as 1/2 ML, were found similar (see Table S3).

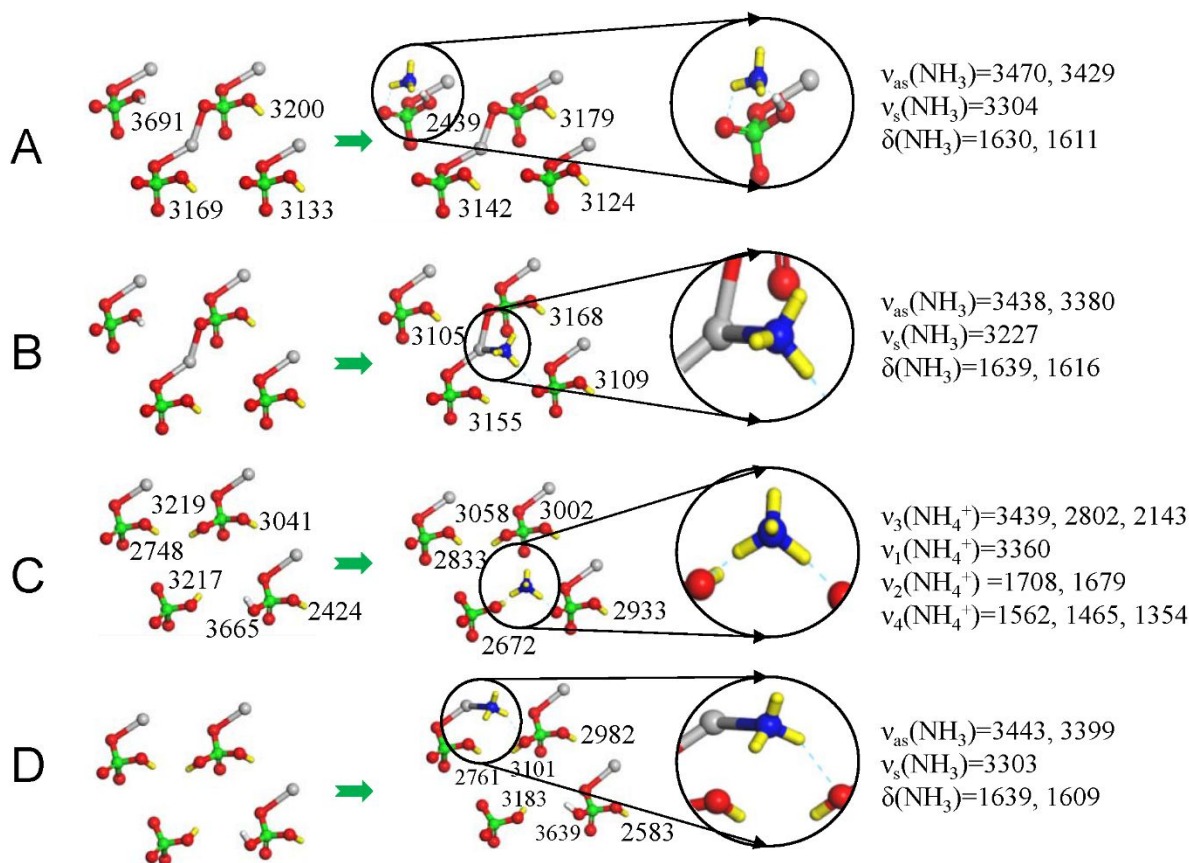


Figure 8. Structures (top view) and computed wavenumbers (in cm⁻¹) of the $\nu(\text{PO-H})$ stretching vibrations and of the NH₃ or NH₄⁺ vibrations after the adsorption of NH₃ on the non-defective dehydrated surface (A and B) and on the defective surface (C and D) at a coverage of $\theta(\text{NH}_3)=1/4$ ML. The corresponding adsorption energies are reported in Table 2. Color-coding: grey for calcium, red for oxygen, green for phosphorus, blue for nitrogen and yellow for hydrogen, except surface H_{up}, which is marked in white.

The negative band at 3670 cm⁻¹ indicated that POH_{up} species are modified by adsorbed NH₃. Thus, the adsorption of NH₃ was considered on the Config 2 of the non-defective surface (see Table 1), which presented some POH_{up} species, and on the defective surface. In both cases, the interaction with the BAS (the POH_{up}) and the LAS (Ca²⁺ in our model that stands for Ba²⁺ in the BaOP catalyst) were considered. The corresponding adsorption energies are provided in Table 2.

Table 2. Adsorption energy of water and ammonia on the non-defective and defective surface corresponding to the structures shown in Figure 8 and Figure 10. The adsorption of ammonia is given as a successive adsorption after the adsorption of water on structures E, F and G.

Label	Surface	Structure description	$E_{\text{ads}}(\text{H}_2\text{O})$	$E_{\text{ads}}(\text{NH}_3)$
			$\text{kJ}\cdot\text{mol}^{-1}$	$\text{kJ}\cdot\text{mol}^{-1}$
A	Non-defective	NH_3 is h-bounded to a P-OH_{up}	-	-48
B	Non-defective	NH_3 is in interaction with Ca^{2+}	-	-89
C	Defective	NH_4^+	-	-118
D	Defective	NH_3 is in interaction with Ca^{2+}	-	-84
E	Non defective	NH_3 is in interaction with Ca^{2+}	-90	-95
F	Non-defective	NH_4^+	-90	-46
G	Defective	NH_4^+	-82	-108

With a low adsorption energy ($-48 \text{ kJ}\cdot\text{mol}^{-1}$), the adsorption on the BAS (structure A) is less likely than on the LAS of the dehydrated non-defective surface (structure B, $-89 \text{ kJ}\cdot\text{mol}^{-1}$). The contrast between these two site types is likely to be reduced since here we modeled Ba^{2+} by a stronger LAS, namely Ca^{2+} . On the defective surface, it was the opposite situation with an adsorption on the LAS (structure D, $-84 \text{ kJ}\cdot\text{mol}^{-1}$) less stabilizing than on the BAS (structure C, $-118 \text{ kJ}\cdot\text{mol}^{-1}$), a difference that is expected to be even stronger for the weak LAS Ba^{2+} . In this defective case, the adsorbed NH_3 even captured

1
2
3 a proton of H_2PO_4^- yielding NH_4^+ , H bonded with several nearby oxygen atoms.
4
5
6
7 Conversely, the generation of NH_4^+ from the proton transfer from HPO_4^{2-} to NH_3 was
8
9
10 found to be very unlikely on the non-defective dehydrated surface with an adsorption
11
12
13 energy much weaker than the non-dissociative adsorption (-12 kJ.mol^{-1} vs. -89 kJ.mol^{-1} ,
14
15
16
17 Figure S5).
18
19

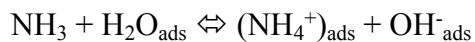
20
21 The experimental spectra contained one band at 1630 cm^{-1} typical of Lewis coordination and/or
22
23 H-bonding ($\delta(\text{NH}_3)$ vibration).⁴⁸ This vibration mode is doubly degenerated in free NH_3 but non-
24
25 symmetric environment slightly split the band in the computed spectra. It was predicted to be not
26
27 sensitive to the type of interaction since it was computed at $1630, 1611 \text{ cm}^{-1}$ when NH_3 was H-
28
29 bonded to P-OH_{up} (Figure 8A) and at $1639, 1609 \text{ cm}^{-1}$ when NH_3 was in interaction with a LAS
30
31 (Figure 8B and D). The $\nu(\text{NH}_3)$ stretching vibrations were more sensitive to the adsorption site.
32
33
34 The symmetric mode was strongly red-shifted (3227 cm^{-1}) when NH_3 was in interaction with the
35
36 LAS on the non-defective surface (Figure 8B) compared with cases where it was in interaction
37
38 with the same site on the defective surface (3303 cm^{-1} , Figure 8D) or H-bonded to PO-H_{up} of the
39
40 non-defective surface (3304 cm^{-1} , Figure 8A). The asymmetric vibrations were all found in a range
41
42 of $3380\text{-}3470 \text{ cm}^{-1}$. All these bands were compatible with the experimental observation of a rather
43
44 complicated $3200\text{-}3400 \text{ cm}^{-1}$ spectral range with bands at $3396, 3375, 3300, 3241$ and 3214 cm^{-1}
45
46 superimposed to an asymmetric broad one (Figure 7). The first two were attributed to $\nu_{\text{asym}}(\text{NH}_3)$
47
48 vibrations and the third one to $\nu_{\text{sym}}(\text{NH}_3)$. Note that $\nu_{\text{asym}}(\text{NH}_3)$ vibrations are doubly degenerated
49
50 for free NH_3 (E mode). Observation of two $\nu_{\text{asym}}(\text{NH}_3)$ bands and one $\nu_{\text{sym}}(\text{NH}_3)$ band implies a
51
52 symmetry lowering compared to C_{3v} . Attribution of the two last bands at 3241 and 3214 cm^{-1} was
53
54
55
56
57
58
59
60

1
2
3 not obvious since it could either correspond to overtones of $\delta_{\text{asym}}(\text{NH}_3)$ and to $\nu_1(\text{NH}_4^+)$
4 vibrations^{49,50} but also to $\nu_{\text{sym}}(\text{NH}_3)$ with NH_3 in interaction with the Lewis site on the non-
5 defective surface (3227 cm^{-1} , Figure 8B) or to $\nu(\text{PO-H})$ vibrations of POH_{down} species. As these
6 bands were kept upon heating to 120 °C while $\nu_4(\text{NH}_4^+)$ at 1475 cm^{-1} ^{49,50} disappeared above 7 °C,
7 attribution to $\nu_1(\text{NH}_4^+)$ was ruled out.
8
9

10
11
12
13
14
15 Observation of broad band tailing to 2400 cm^{-1} strongly suggested higher contribution of $\nu(\text{PO-}$
16 H) vibrations due to POH_{down} . Indeed, some POH_{down} vibrations were predicted to be red-shifted
17 by the NH_3 absorption with bands shifting from 3169 to 3139 cm^{-1} for instance (see Figure 8A).
18 In addition, the presence of Ca^{2+} vacancies in the defective structure would also yield to the
19 observation of vibrations as low as 2583 cm^{-1} related to the presence of H_2PO_4^- species (Figure
20 8D). Last, when NH_3 was H bonded directly to PO-H_{up} (Figure 8A), the $\nu(\text{PO-H}_{\text{up}})$ band at 3691
21 cm^{-1} shifted down to 2439 cm^{-1} due to the strong H-bond. This corresponds to a zone where a small
22 absorbance was seen in the experimental spectra. The orientation of the PO-H_{up} was also affected
23 in the case of an interaction of NH_3 with the LAS, despite the lack of direct interaction. It rotated
24 from up to down, inducing a strong red shift of $\nu(\text{PO-H}_{\text{up}})$ from 3691 to 3105 cm^{-1} and the red shift
25 of the three $\nu(\text{PO-H}_{\text{down}})$ to 3100-3200 cm^{-1} as shown in Figure 8B and D. This is in line with the
26 experimental observations regarding the disappearing of the band at 3670 cm^{-1} and the broad band
27 in the range of 2800-3200 cm^{-1} . Finally, the band at 3241 cm^{-1} could correspond to the $\nu_{\text{sym}}(\text{NH}_3)$
28 vibration of NH_3 adsorbed on the LAS of the non-defective surface while the shoulder at 3214
29 cm^{-1} would be assigned to changes in the POH_{down} signature. Attribution of the bands 3241 and
30 3214 cm^{-1} to two different species (adsorbed NH_3 and POH_{down} , respectively) was confirmed by
31 the change of their relative intensity with the temperature (Figure 7).
32
33
34
35
36
37
38
39
40
41
42
43
44
45
46
47
48
49
50
51
52
53

54
55 The negative shoulder observed at 3715 cm^{-1} only on the spectrum recorded to 7 °C (below
56
57

1
2
3 RT) was assigned to $\nu(\text{H}_2\text{O})$ due to traces of physisorbed water leading to the spontaneous
4
5 reaction:^{16,39}
6



7
8
9
10 Such reaction which did occur only at 7 °C also explained observation of the bending $\nu_4(\text{NH}_4^+)$
11
12 and $\nu_2(\text{NH}_4^+)$ vibrations bands at 1475 and 1685 cm^{-1} , respectively.^{49,50} The latter one is observed
13
14 by IR only when symmetry of NH_4^+ cations is lower than T_d .^{49,50} DFT computations provided
15
16 another possible explanation on NH_4^+ formation. Indeed, traces of physisorbed water at low
17
18 temperature could increase the amount of Ca^{2+} vacancies (see section 3.2), which promotes the
19
20 formation of NH_4^+ . Their presence was predicted on the defective surface, with strong adsorption
21
22 energy of -118 $\text{kJ}\cdot\text{mol}^{-1}$ (Table 2). The computed NH_4^+ vibration bands were split by the
23
24 environment. By comparison with the observed ones (1475 and 1685 cm^{-1}), two bands were found
25
26 to be the major ones (1465 and 1679 cm^{-1} , see Figure 8C).
27
28
29
30

31 To sum up, the interaction of NH_3 with the POH groups by H-bonding without significant
32
33 protonation of the non-defective surface could not be discarded based on the infrared signature.
34
35 However, it was found to be less likely based on energetic consideration since it had the weakest
36
37 adsorption energy (Table 2). Even upon interaction with the LAS, the $\nu(\text{PO-H}_{\text{up}})$ band was found
38
39 to disappear due to the re-orientation of the PO-H bond downward. Bands at 3396-3375, 3300,
40
41 3241 and 3214 cm^{-1} were attributed to degenerated $\nu_{\text{asym}}(\text{NH}_3)$, $\nu_{\text{sym}}(\text{NH}_3)$ of NH_3 in interaction
42
43 with the LAS of the defective surface, $\nu_{\text{sym}}(\text{NH}_3)$ of NH_3 in interaction with the LAS of the non-
44
45 defective surface and to $\nu(\text{PO-H}_{\text{down}})$ respectively. The broad band tailing at 2400 cm^{-1} was due to
46
47 the reorganization of the $\text{PO-H}_{\text{down}}$ upon adsorption.
48
49
50
51
52
53
54

55 **3.4 Water effect on acidity**

56
57
58
59
60

In situ acidity measurements were achieved at adsorption equilibrium under 1%NH₃-3%H₂O-He flow and FTIR spectra are plotted in Figure 9. The absorbance value of the $\nu_4(\text{NH}_4^+)$ band at 1458 cm⁻¹ was strongly increased evidencing a higher Brønsted acidity formed under water vapor.^{20,39} As the band at 1640 cm⁻¹ could be attributed to either $\delta(\text{NH}_3)$ and $\delta(\text{H}_2\text{O})$ vibrations and as no $\nu_{\text{asym}}(\text{NH}_3)$ vibrations around 3300-3400 cm⁻¹ were distinguishable from the broad band at 3420 cm⁻¹ due to $\nu(\text{H}_2\text{O})$ of chemisorbed water, the presence of chemisorbed NH₃ species remained questionable. Note that the shoulder observable at 3220 cm⁻¹ above 40 °C could be attributed to $\nu_1(\text{NH}_4^+)$ vibrations associated with $\nu_4(\text{NH}_4^+)$ at 1458 cm⁻¹.^{49,50} Finally, the small band at 3692 cm⁻¹ can correspond to $\nu(\text{PO-H}_{\text{up}})$ and to $\nu(\text{H}_2\text{O}_{\text{ads}})$ as already discussed earlier.

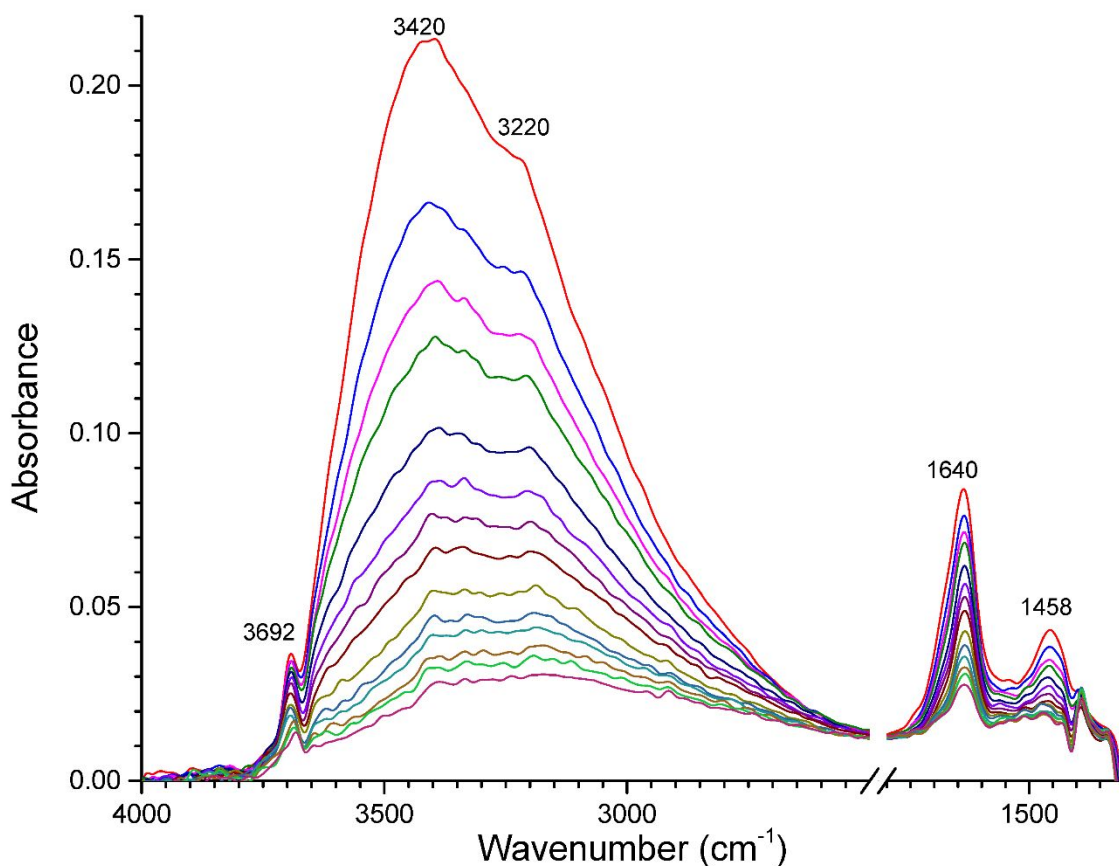


Figure 9. Evolution of the IR bands of NH_3 adsorbed species on pre-treated BaOP catalyst recorded under 1% NH_3 -3% H_2O -He flow from 172 to 28 °C. The backgrounds correspond to the spectra recorded after pretreatment under He flow at the same temperatures, mass of the pellet 53 mg.

DFT computations provided an atomistic view of the adsorption of ammonia on the BAS and the LAS of both the non-defective and defective surface, but including water co-adsorption ($\theta(\text{H}_2\text{O})=1/8$ ML) assuming that the presence of ammonia does not modify strongly the predicted water coverage. The corresponding structures along with their wavenumbers are shown in Figure 10 and the adsorption energies are reported in Table 2. The computed vibrations of the three structures are compatible with the experimental observations.

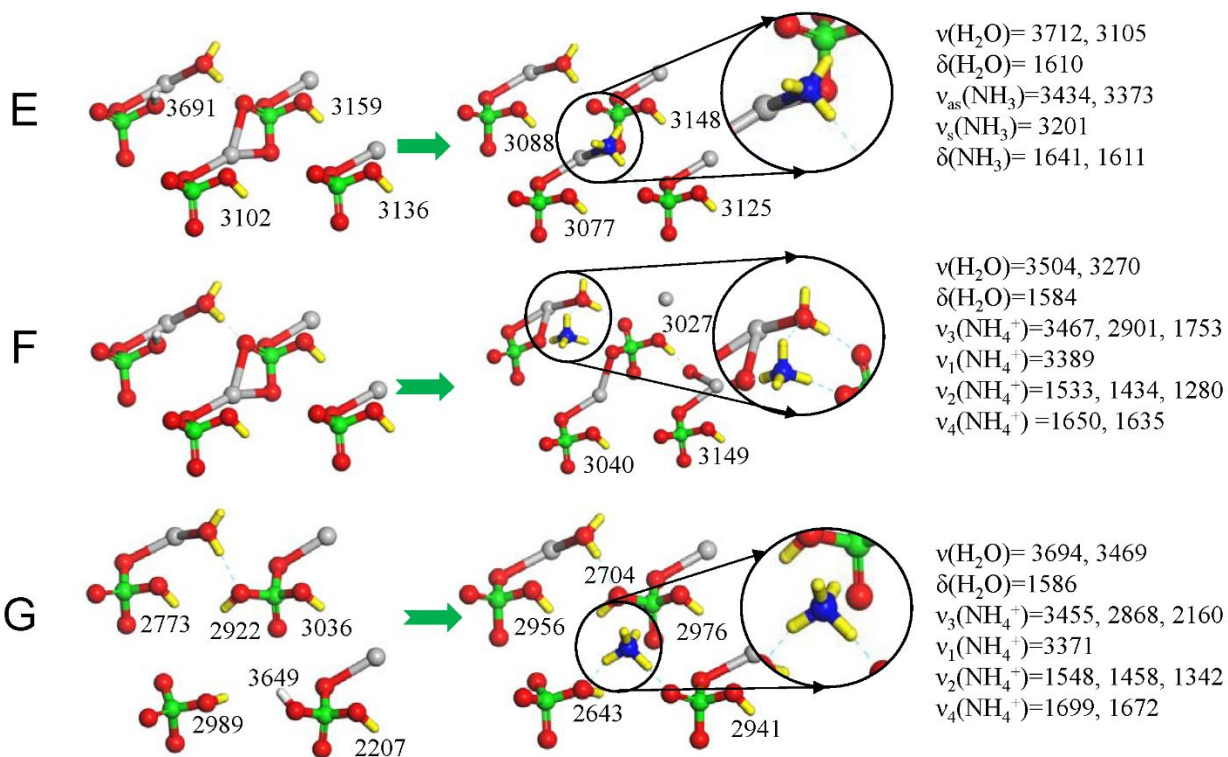


Figure 10. Structures and computed wavenumbers (in cm^{-1}) of the $\nu(\text{PO-H})$ stretching vibrations, water vibration and of the NH_3 or NH_4^+ vibration after the adsorption of NH_3 on the non-defective dehydrated surface (E and F) and on the defective surface (G). The corresponding adsorption energies are reported in Table 2. Color-coding: grey for

1
2
3 calcium, red for oxygen, green for phosphorus, blue for nitrogen and yellow for hydrogen, except surface H_{up} which
4 is marked in white.
5
6
7
8

9 On the non-defective surface, the presence of a water molecule does not modify the interaction of
10 NH₃ with the LAS site (structure E), which was still found being the most stable adsorption site
11 with adsorption energy of -95 kJ.mol⁻¹ (Table 2). Noticeably, the P-OH_{up} shifts to a P-OH_{down}
12 during this adsorption despite the absence of a direct interaction with NH₃, yielding to a predicted
13 disappearance of the vibration at 3691 cm⁻¹ but with the appearance of a band at 3712 cm⁻¹ related
14 to the elongation of OH in the chemisorbed water. In other words, while the presence of NH₃ was
15 questionable based on the experimental spectrum, it seems rather likely at distance of defective
16 sites since structure E is more stable than the ones yielding to ammonium following a proton
17 transfer from water or the BAS of the surface. Still, co-adsorbed water made the BAS more acidic.
18 Indeed, interaction of NH₃ with the PO-H_{up} generated NH₄⁺ (structure F) with adsorption energy
19 of -46 kJ.mol⁻¹ (Table 2), a process strongly facilitated by the presence of water even if it does not
20 participate directly, thanks to an extra stabilizing H bond. On the totally dehydrated surface, the
21 same reactive adsorption yielded only to adsorption energy of -22 kJ.mol⁻¹. This could explain the
22 increase of the NH₄⁺ band absorption in presence of ammonia co-fed with water in comparison
23 with ammonia only. Another source of NH₄⁺ could be the increase of Ca²⁺ vacancies promoted by
24 the presence of water (see section 3.2) since NH₃ easily turns into NH₄⁺ by capturing the proton of
25 the H₂PO₄⁻ group close to the Ca²⁺ vacancy (structure G), with strong adsorption energy of -108
26 kJ.mol⁻¹ (Table 2).
27
28
29
30
31
32
33
34
35
36
37
38
39
40
41
42
43
44
45
46
47
48
49
50
51
52

53 4. CONCLUSIONS 54 55 56 57 58 59 60

1
2
3 In this work, acidic properties of BaOP catalyst were investigated combining FTIR spectra
4 achieved at the dehydrated state and under water vapour and DFT calculations. Such catalyst
5 efficient for the dehydration of lactic acid to acrylic acid was previously shown to contain a surface
6 mono/dihydrogen phosphate amorphous layer composed by Ba^{2+} cations, P=O and POH groups.
7 Therefore, the surface layer was simulated by non-defective and defective MPOH structure.
8 Adsorption of pyridine, lutidine and NH_3 at the surface of BaOP catalyst revealed the presence of
9 moderate LAS and of POH groups without significant protonation for the first two probe
10 molecules. Ammonia was found to mainly interact with the LAS on both the non-defective surface
11 and the defective surface while the PO- H_{up} surface groups are reoriented downward. Formation of
12 BAS was shown to occur under water vapor by co-adsorption of NH_3 and H_2O . The phenomenon
13 cannot be explained by dissociation of H_2O molecules as shown by DFT calculations. In fact, the
14 presence of water does not modify the interaction of NH_3 with the LAS sites of non-defective
15 surface but made the BAS more acidic. The presence of water could also promote formation of
16 defective surface and hence H_2PO_4^- groups which easily react with NH_3 to form NH_4^+ .
17
18
19
20
21
22
23
24
25
26
27
28
29
30
31
32
33
34
35
36

37 ASSOCIATED CONTENT

38
39 The Supporting Information is available free of charge on the ACS Publications website at DOI:
40 XXX
41

42 Scaling factor of NH_3 vibrational modes, Influence of the PO-H orientation in the non-defective
43 partially hydrated (010) surface ($\theta(\text{H}_2\text{O})=1/8$ ML) on the stability at 380 °C and the computed
44 wavenumbers of $\nu(\text{PO-H})$, wavenumbers of NH_3 and NH_4^+ co-adsorption on defective surface,
45 dissociated H_2O on defective surface, Structure of the dissociated H_2O on the non-defective
46 surface, FTIR spectrum of adsorbed pyridine, Experimental evolutions of the coverage of the NH_3
47 adsorbed species with the adsorption temperature and theoretical curve obtained using Temkin
48
49
50
51
52
53
54
55
56
57
58
59
60

1
2
3 model; surface energy in eV/Å² of Brushite (010) surfaces with various coverages; possible
4 configuration of the ammonium cation on a dehydrated surface; archive of raw data from
5
6 computations including structures and frequencies.
7
8
9

10 11 12 13 **AUTHOR INFORMATION**

14 15 **Corresponding Authors**

16
17 *E-mail: stephane.loridant@ircelyon.univ-lyon1.fr

18
19 *E-mail: carine.michel@ens-lyon.fr

20 21 22 **ORCID**

23 Stéphane Loridant: 0000-0001-8590-433X

24 Carine Michel: 0000-0002-4501-7194

25 26 27 **Notes**

28
29 The authors declare no competing financial interest.
30
31
32

33 34 **ACKNOWLEDGEMENTS**

35
36 This work was supported by French ANR Program Chimie Durable–Industries–Innovation (CD2I)

37
38 GALAC, a joint project between IRCELYON, UCCS, LC/ENS-Lyon and Novance company.

39
40 Laurent Piccolo is acknowledged for access to the IR apparatus founded by the project DINAMIC
41
42 (reference ANR-2011-BS10-009).
43
44
45
46
47
48
49
50
51
52
53
54
55
56
57
58
59
60

REFERENCES

- (1) Mäki-Arvela, P.; Simakova, I.L.; Salmi, T.; Murzin, D.Y. Production of lactic acid/lactates from biomass and their catalytic transformations to commodities. *Chem. Rev.* **2013**, *114*, 1909–1971.
- (2) Blanco, E.; Loridant, S.; Pinel, C. Valorization of lactic acid and derivatives to acrylic acid derivatives: review of mechanistic studies. In *Reaction Pathways and Mechanisms in Thermocatalytic Biomass Conversion II*, Schlaf, M.; Zhang, Z. C., Eds.; Springer, 2016, Chapter 3, pp39–62.
- (3) Sun, D.; Yamada, Y.; Sato, S.; Ueda, W. Glycerol as a potential renewable raw material for acrylic acid production. *Green Chem.* **2017**, *19*, 3186–3213.
- (4) Chierogato, A.; Soriano, M.D.; Basile, F.; Liosi, G.; Zamora, S.; Concepcion, P.; Cavani, F. Lopez Nieto, J.M. One-pot glycerol oxydehydration to acrylic acid on multifunctional catalysts: Focus on the influence of the reaction parameters in respect to the catalytic performance. *Appl. Catal. B: Environ.* **2014**, *150-151*, 37–46.
- (5) Chierogato, A.; Soriano, M.D.; Garcia-Gonzalez, E.; Puglia, G.; Basile, F.; Concepcion, P.; Bandinelli, C.; Lopez Nieto, J.M.; Cavani, F. Multielement Crystalline and Pseudocrystalline Oxides as Efficient Catalysts for the Direct Transformation of Glycerol into Acrylic Acid. *ChemSusChem* **2015**, *8*, 398-406.
- (6) Fan, Y.; Zhou, C.; Zhu, X. Selective Catalysis of Lactic Acid to Produce Commodity Chemicals, *Catal. Rev.* **2009**, *51*, 293–324.
- (7) Abdel-Rahman, M.A.; Tashiro, Y.; Sonomoto, K. Lactic acid production from lignocellulose-derived sugars using lactic acid bacteria: Overview and limits. *BioTech. Adv.* **2013**, *1*, 877–902.
- (8) Abdel-Rahman, M.A.; Tashiro, Y.; Sonomoto, K. Recent advances in lactic acid production by microbial fermentation processes. *J. Biotech.* **2011**, *156*, 286–301.

- 1
2
3 (9) Auneau, F.; SadrArani, L.; Besson, M.; Djakovitch, L.; Michel, C.; Delbecq, F.; Sautet, P.;
4 Pinel, C.; Heterogeneous Transformation of Glycerol to Lactic Acid. *Top.Catal.* **2012**, *55*, 474.
5
6
7 (10) [https://www.businesswire.com/news/home/20170621005594/en/Global-Lactic-Acid-](https://www.businesswire.com/news/home/20170621005594/en/Global-Lactic-Acid-Market-2017-2025---Growth)
8 [Market-2017-2025---Growth](https://www.businesswire.com/news/home/20170621005594/en/Global-Lactic-Acid-Market-2017-2025---Growth)
9
10
11 (11) Blanco, E.; Delichere, P.; Millet, J.M.M.; Loridant, S. Gas phase dehydration of lactic acid to
12 acrylic acid over alkaline-earth phosphates catalyts. *Catal. Today*, **2014**, *226*, 185–191.
13
14 (12) Blanco, E.; Lorentz, C.; Delichere, P.; Burel, L.; Vrinat, M.; Millet, J.M.M.; Loridant, S.
15 Dehydration of ethyl lactate over alkaline earth phosphates: Performances, effect of water on
16 reaction pathways and active sites, *Appl. Catal. B: Environ.* **2016**, *180*, 596–606.
17
18 (13) Hammaeher, C.; Paul, J.-F. Density functional theory study of lactic acid adsorption and
19 dehydration reaction on monoclinic 011, $\bar{1}01$, and $\bar{1}11$ zirconia surfaces. *J. Catal.* **2013**, *300*, 174–
20 182.
21
22 (14) Dorozhkin S.V.; Epple, M. Biological and Medical Significance of Calcium Phosphates,
23 *Angew. Chem. Int. Ed.* **2002**, *41*, 3130 – 3146.
24
25 (15) Chafik, T.; Dulaurent, O.; Gass, J.L.; Bianchi, D. Heat of Adsorption of Carbon Monoxide
26 on a Pt/Rh/CeO₂/Al₂O₃ Three-Way Catalyst Using in-Situ Infrared Spectroscopy at High
27 Temperatures. *J. Catal.* **1998**, *179*, 503–514.
28
29 (16) Giraud, F.; Couble, J.; Geantet, C.; Guilhaume, N.; Puzenat, E.; Gros, S.; Porcheron, L.;
30 Kanneche, M.; Bianchi, D. Experimental Microkinetic Approach of De-NO_x by NH₃ on
31 V₂O₅/WO₃/TiO₂ Catalysts. 4. Individual Heats of Adsorption of Adsorbed H₂O Species on Sulfate-
32 Free and Sulfated TiO₂ Supports. *J. Phys. Chem.C* **2015**, *119*, 16089–16105.
33
34 (17) Giraud, F.; Geantet, C.; Guilhaume, N.; Gros, S.; Porcheron, L.; Kanneche, M.; Bianchi, D.
35 Experimental Microkinetic Approach of De-NO_x by NH₃ on V₂O₅/WO₃/TiO₂ Catalysts. 1.
36
37
38
39
40
41
42
43
44
45
46
47
48
49
50
51
52
53
54
55
56
57
58
59
60

1
2
3 Individual Heats of Adsorption of Adsorbed NH₃ Species on a Sulfate-Free TiO₂ Support Using
4 Adsorption Isobars. *J. Phys. Chem. C* **2014**, *118*, 15664–15676.

5
6
7 (18) Giraud, F.; Geantet, C.; Guilhaume, N.; Loridant, S.; Gros, S.; Porcheron, L.; Kanniche, M.;
8 Bianchi, D. Experimental Microkinetic Approach of De-NO_x by NH₃ on V₂O₅/WO₃/TiO₂
9 Catalysts. 2. Impact of Superficial Sulfate and/or V_xO_y groups on the Heats of Adsorption of
10 Adsorbed NH₃ Species. *J. Phys. Chem. C* **2014**, *118*, 15677–15692.

11
12
13 (19) Giraud, F.; Geantet, C.; Guilhaume, N.; Loridant, S.; Gros, S.; Porcheron, L.; Kanniche, M.;
14 Bianchi, D. Experimental Microkinetic Approach of De-NO_x by NH₃ on V₂O₅/WO₃/TiO₂
15 Catalysts. 3. Impact of Superficial WO_z and V_xO_y/WO_z Groups on the Heats of Adsorption of
16 Adsorbed NH₃ Species. *J. Phys. Chem. C* **2015**, *119*, 15401–15413.

17
18 (20) Buniazet, Z.; Couble, J.; Bianchi, D.; Rivallan, M.; Cabiach, A.; Maury, S.; Loridant, S.
19 Unravelling water effects on solid acid catalysts: Case study of TiO₂/SiO₂ as a catalyst for the
20 dehydration of isobutanol, *J. Catal.* **2017**, *348*, 125–134.

21
22 (21) Kresse, G.; Furthmüller, J. Efficient iterative schemes for ab initio total-energy calculations
23 using a plane-wave basis set. *Phys. Rev. B-Condens. Matter Mater. Phys.* **1996**, *54*, 11169–11186.

24
25 (22) Kresse, G.; Furthmüller, J. Efficiency of ab-initio total energy calculations for metals and
26 semiconductors using a plane-wave basis set. *Comput. Mater. Sci.* **1996**, *6*, 15–50.

27
28 (23) Kresse, G.; Hafner, J. *Ab initio* molecular dynamics for liquid metals. *Phys. Rev. B - Condens.*
29 *Matter Mater. Phys.* **1993**, *47*, 558–561.

30
31 (24) Perdew, J. P.; Burke, K.; Ernzerhof, M. Generalized Gradient Approximation Made Simple.
32 *Phys. Rev. Lett.* **1996**, *77*, 3865–3868.

33
34 (25) Kresse, G.; Joubert, D. From ultrasoft pseudopotentials to the projector augmented-wave
35 method. *Phys. Rev. B-Condens. Matter Mater. Phys.* **1999**, *59*, 1758–1775.

- 1
2
3 (26) Curry, N.A.; Jones, D. W. Crystal Structure of Brushite, Calcium Hydrogen Orthophosphate
4 Dihydrate: A Neutron-diffraction Investigation. *J. Chem. Soc. A* **1971**, 3725–3729.
5
6
7 (27) Hirsch, A., Azuri, I., Addadi, L., Weiner, S., Yang, K., Curtarolo, S., Kronik, L. Infrared
8 Absorption Spectrum of Brushite from First Principles. *Chem. Mater.* **2014**, 26, 2934-2942.
9
10 (28) Schofield, P.F.; Knight, K.S.; van der Houwen, J.A.M.; Valsami-Jones, E. The role of
11 hydrogen bonding in the thermal expansion and dehydration of brushite, di-calcium phosphate
12 dihydrate *Phys. Chem. Minerals* **2004**, 31, 606–624.
13
14 (29) Kumta, P.N.; Sfeir, C.; Lee, D.-H.; Olton, D.; Choi, D. Nanostructured calcium phosphates
15 for biomedical applications: novel synthesis and characterization, *Acta Biomaterialia*, **2005**, 1, 65–
16 83.
17
18 (30) Baroni, S.; Giannozzi, P.; Testa, A. Green's-Function Approach to Linear Response in Solids.
19 *Phys. Rev. Lett.* **1987**, 58, 1861–1894.
20
21 (31) Bauer, T.; Maisel, S.; Blaumeiser, D.; Vecchietti, J.; Taccardi, N.; Wasserscheid, P.;
22 Bonivardi, A.; Görling, A.; Libuda, J. *ACS Catal.* **2019**, 9, 2842–2853.
23
24 (32) Anggara, T.; Paolucci, C.; Schneider, W.F. *J. Phys. Chem. C* **2016**, 120, 27934–27943.
25
26 (33) Chizallet, C.; Costentin, G. ; Che, M. ; Delbecq, F. ; Sautet, P. *J. Am. Chem. Soc.* **2007**, 129,
27 6442-6452.
28
29 (34) Cheng, Z.H.; Yasukawa, A.; Kandori, K.; Ishikawa, T. FTIR Study on incorporation of CO₂
30 into calcium hydroxyapatite. *J. Chem. Soc., Faraday Trans.* **1998**, 94, 1501–1505.
31
32 (35) Trchova, M.; Capkova, P.; Matejka, P.; Melanova, K.; Benes, L. Study of Host–Guest
33 Interactions in Intercalate Zr(HPO₄)₂·2CH₃CH₂OH using a Combination of Vibration
34 Spectroscopy and Molecular Simulations. *J. Solid State Chem.* **1999**, 145, 1–9.
35
36 (36) Koleva, V.; Stefov, V.; Cahil, A.; Najdoski, M.; Soptrajanov, B.; Engelen, B.; Lutz, H.D.
37
38
39
40
41
42
43
44
45
46
47
48
49
50
51
52
53
54
55
56
57
58
59
60

Infrared and Raman studies of manganese dihydrogen phosphate dihydrate, $\text{Mn}(\text{H}_2\text{PO}_4)_2 \cdot 2\text{H}_2\text{O}$.

Part II: Region of the internal OH group vibrations. *J. Mol. Struct.* **2009**, *919*, 164–169.

(37) Frost, R.L.; Xi, Y.; Palmer, S.J.; Tan, K. Millar, G.J. Vibrational spectroscopy of synthetic archerite $(\text{K},\text{NH}_4)\text{H}_2\text{PO}_4$ and in comparison with the natural cave mineral. *J. Mol. Struct.* **2012**, *1011*, 128–133.

(38) Frost, R.L.; Palmer, S.J.; Xi, Y. A Raman spectroscopic study of the mono-hydrogen phosphate mineral dorfmanite $\text{Na}_2(\text{PO}_3\text{OH}) \cdot 2\text{H}_2\text{O}$ and in comparison with brushite. *Spectrochim. Acta Part A* **2011**, *82*, 132–136.

(39) Giraud, F.; Couble, J.; Geantet, C.; Guilhaume, N.; Puzenat, E.; Gros, S.; Porcheron, L.; Kanniche, M.; Bianchi, D. Experimental Microkinetic Approach of De-NO_x by NH₃ on V₂O₅/WO₃/TiO₂ Catalysts. 4. Individual Heats of Adsorption of Adsorbed H₂O Species on Sulfate-Free and Sulfated TiO₂ Supports. *J. Phys. Chem. C* **2015**, *119*, 16089–16105.

(40) Buniazet, Z.; A. Cabiac, S. Maury, D. Bianchi, S. Loridant, Unexpected selectivity of ferrierite for the conversion of isobutanol to linear butenes and water effects, *Appl. Catal. B: Environmental* **2019**, *243*, 594–603.

(41) Dosen, A.; Giese, R.F. Thermal decomposition of brushite, $\text{CaHPO}_4 \cdot 2\text{H}_2\text{O}$ to monetite CaHPO_4 and the formation of an amorphous phase, *American Mineralogist*, **2011**, *96*, 368–373.

(42) Lagno, F.; Rocha, S.D.F; Katsarou, L.; Demopoulos, G.P. Supersaturation-Controlled Synthesis of Dicalcium Phosphate Dihydrate and Nanocrystalline Calcium-Deficient Hydroxyapatite, *Ind. Eng. Chem. Res.* **2012**, *51*, 6605–6612.

(43) Wang, L.; Nancollas, G.H. Calcium Orthophosphates: Crystallization and Dissolution, *Chem. Rev.* **2008**, *108*, 4628–4669.

(44) Busca, G. The surface acidity of solid oxides and its characterization by IR spectroscopic

1
2
3 methods. An attempt at systematization *Phys. Chem. Chem. Phys.* **1999**, *1*, 723–736.

4
5 (45) Busca, G. Spectroscopic characterization of the acid properties of metal oxide catalysts. *Catal.*
6
7 *Today* **1998**, *41*, 191–206.

8
9
10 (46) Oliviero, L.; Vimont, A.; Lavalley, J.-C.; Romero Sarria, F.; Gaillard, M.; Mauge, F. 2,6-
11
12 Dimethylpyridine as a probe of the strength of Brønsted acid sites: study on zeolites. Application
13
14 to alumina. *Phys. Chem. Chem. Phys.* **2005**, *7*, 1861–1869.

15
16
17 (47) Onfroy, T.; Clet, G.; Houalla, M. Quantitative IR characterization of the acidity of various
18
19 oxide catalysts. *Micropor. Mesopor. Mater.* **2005**, *82*, 99–104.

20
21 (48) Giraud, F.; Geantet, C.; Guilhaume, N.; Loridant, S.; Gros, S.; Porcheron, L.; Kanniche, M.;
22
23 Bianchi, D. Experimental Microkinetic Approach of De-NO_x by NH₃ on V₂O₅/WO₃/TiO₂
24
25 Catalysts. 1. Individual Heats of Adsorption of Adsorbed NH₃ Species on a Sulfate-Free TiO₂
26
27 Support Using Adsorption Isobars. *J. Phys. Chem. C* **2014**, *118*, 15677–15692.

28
29 (49) Zecchina, A.; Marchese, L.; Bordiga, S.; Pazè, C.; Gianotti, E. Vibrational Spectroscopy of
30
31 NH₄⁺ Ions in Zeolitic Materials: An IR Study. *J. Phys. Chem. B* **1997**, *101*, 10128–10135.

32
33
34 (50) Plaza, I.; Rubin, J.; Laguna, M.A.; Bartolomé, J. Optical spectroscopy of the NH₄⁺ internal
35
36 vibrations in the orthorhombic phase of NH₄MF₃ (M is Mn, Zn) perovskites. *Spectrochimica Acta*
37
38 *Part A* **1996**, *52*, 57–67.
39
40
41
42
43
44
45
46
47
48
49
50
51
52
53
54
55
56
57
58
59
60

FIGURES CAPTIONS

Figure 1: *In situ* DRIFT spectra of BaOP at 380 °C under He, 30% H_2O -He and 30% D_2O -He. The background corresponds to the spectrum of dehydrated KBr.

Figure 2: Unit cell of the layered structure of the Brushite, containing Ca atoms (grey), O atoms (red), H atoms (yellow) and P atoms (green).

Figure 3: Structures of the (010) surface of $\text{CaHPO}_4 \cdot n\text{H}_2\text{O}$ with different water coverages, θ (H_2O)=1 ML, 7/8 ML, 1/8 ML and 0 ML. Only half of the surface structure is shown here for simplicity. The two different types of water molecules are marked as W_a and W_b highlighted by a black circle in the top left structure, which corresponds to the structure obtained as cleaved from the bulk. The H bond network of W_a and W_b is shown in light blue dashed lines. At 1ML, 8 water molecules are found. At 7/8ML, one W_b water has been removed and the black circle indicates its former position. At 1/8ML, only one water molecule remains (W_a type) as highlighted by a black circle. Color-coding: grey for calcium, red for oxygen, green for phosphorus and yellow for hydrogen.

Figure 4: Surface energy in $\text{eV}/\text{\AA}^2$ of Brushite (010) surfaces with various coverages ($\theta(\text{H}_2\text{O})=1$ ML, 7/8 ML, 1/8 ML and 0 ML) in water as function of the temperature and under a pressure in water of 1 atm.

Figure 5: Computed structure of the defective surface. The Ca^{2+} vacancy is shown with a blue circle, the H_{down} with a pink dashed circle and H_{up} with a pink solid circle. The calculated wavenumbers (after rescaling as mentioned in the 2.3 section) of $\nu(\text{PO-H})$ vibrations on the first layer are also shown nearby in cm^{-1} . Color-coding: grey for calcium, red for oxygen, green for phosphorus and yellow for hydrogen, except surface H_{up} , which is marked in white.

1
2
3 **Figure 6:** Evolution of the FTIR spectra of BaOP after adsorption of lutidine and desorption under
4 vacuum at increasing temperature.
5
6

7 **Figure 7:** Evolution of the IR bands of NH_3 adsorbed species on pre-treated BaOP catalyst
8 recorded under 2% NH_3 -He flow from 120 to 7 °C. The backgrounds correspond to the spectra
9 recorded after pretreatment under He flow at the same temperatures, mass of the pellet 53 mg.
10
11
12

13 **Figure 8:** Structures (top view) and computed wavenumbers (in cm^{-1}) of the $\nu(\text{PO-H})$ stretching
14 vibrations and of the NH_3 or NH_4^+ vibrations after the adsorption of NH_3 on the non-defective
15 dehydrated surface (A and B) and on the defective surface (C and D) at a coverage of $\theta(\text{NH}_3)=1/4$
16 ML. The corresponding adsorption energies are reported in Table 2. Color-coding: grey for
17 calcium, red for oxygen, green for phosphorus, blue for nitrogen and yellow for hydrogen, except
18 surface H_{up} , which is marked in white.
19
20
21
22
23
24
25
26
27

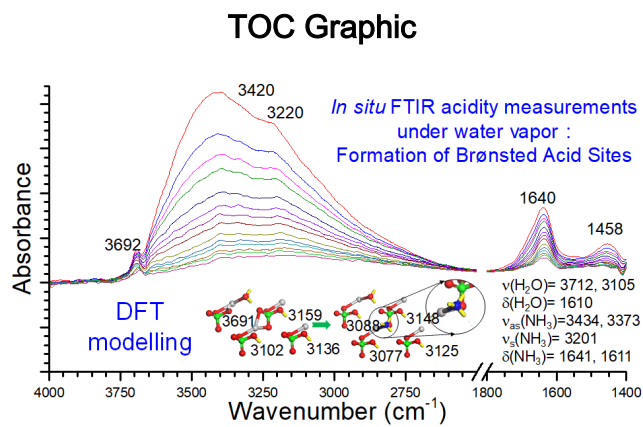
28 **Figure 9:** Evolution of the IR bands of NH_3 adsorbed species on pre-treated BaOP catalyst
29 recorded under 1% NH_3 -3% H_2O -He flow from 172 to 28 °C. The backgrounds correspond to the
30 spectra recorded after pretreatment under He flow at the same temperatures, mass of the pellet 53
31 mg.
32
33
34
35
36
37
38

39 **Figure 10:** Structures and computed wavenumbers (in cm^{-1}) of the $\nu(\text{PO-H})$ stretching vibrations,
40 water vibration and of the NH_3 or NH_4^+ vibration after the adsorption of NH_3 on the non-defective
41 dehydrated surface (E and F) and on the defective surface (G). The corresponding adsorption
42 energies are reported in Table 2. Color-coding: grey for calcium, red for oxygen, green for
43 phosphorus, blue for nitrogen and yellow for hydrogen, except surface H_{up} , which is marked in
44 white.
45
46
47
48
49
50
51
52
53
54
55
56
57
58
59
60

1
2
3 **TABLES CAPTIONS**
4
5

6 **Table 1:** Influence of the PO-H orientation in the non-defective dehydrated (010) surface of
7
8 Brushite on the stability at 380 °C and the computed wavenumbers of $\nu(\text{PO-H})$, reported after
9
10 rescaling as mentioned in the 2.3 section.
11
12

13
14
15 **Table 2:** Adsorption energy of water and ammonia on the non-defective and defective surface
16
17 corresponding to the structures shown in Figure 8 and Figure 10. The adsorption of ammonia is
18
19 given as a successive adsorption after the adsorption of water on structures E, F and G.
20
21
22
23
24
25
26
27
28
29
30
31
32
33
34
35
36
37
38
39
40
41
42
43
44
45
46
47
48
49
50
51
52
53
54
55
56
57
58
59
60



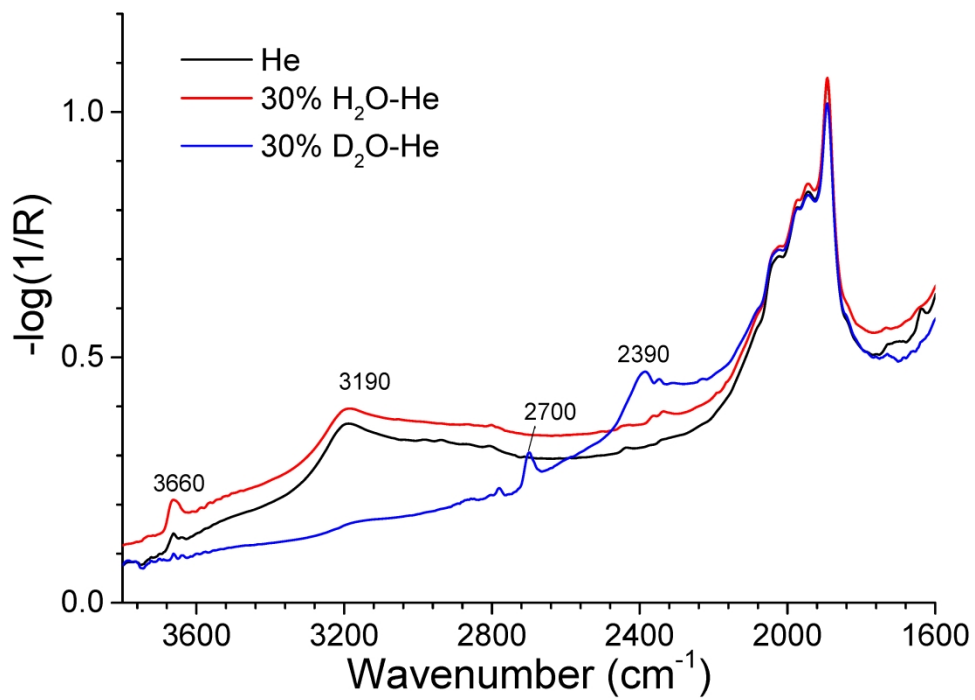


Figure1

297x210mm (300 x 300 DPI)

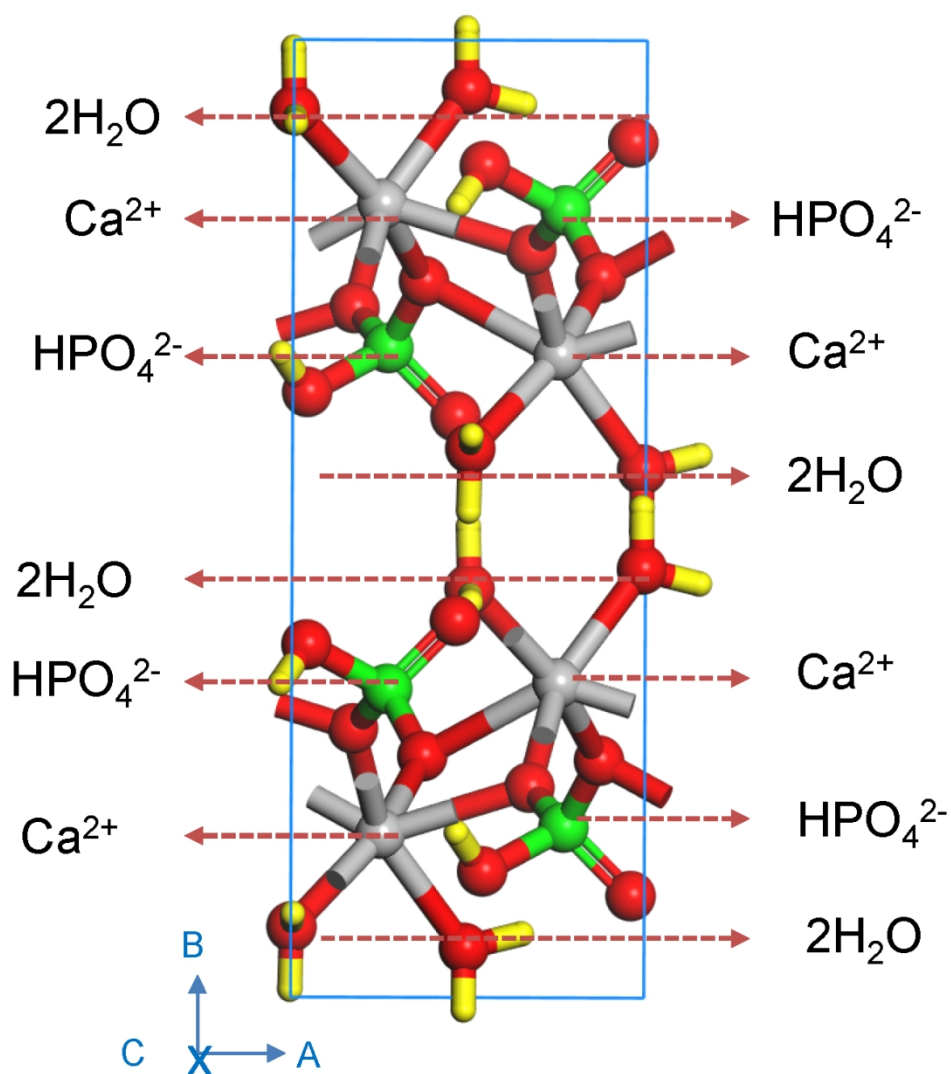


Figure2

117x132mm (300 x 300 DPI)

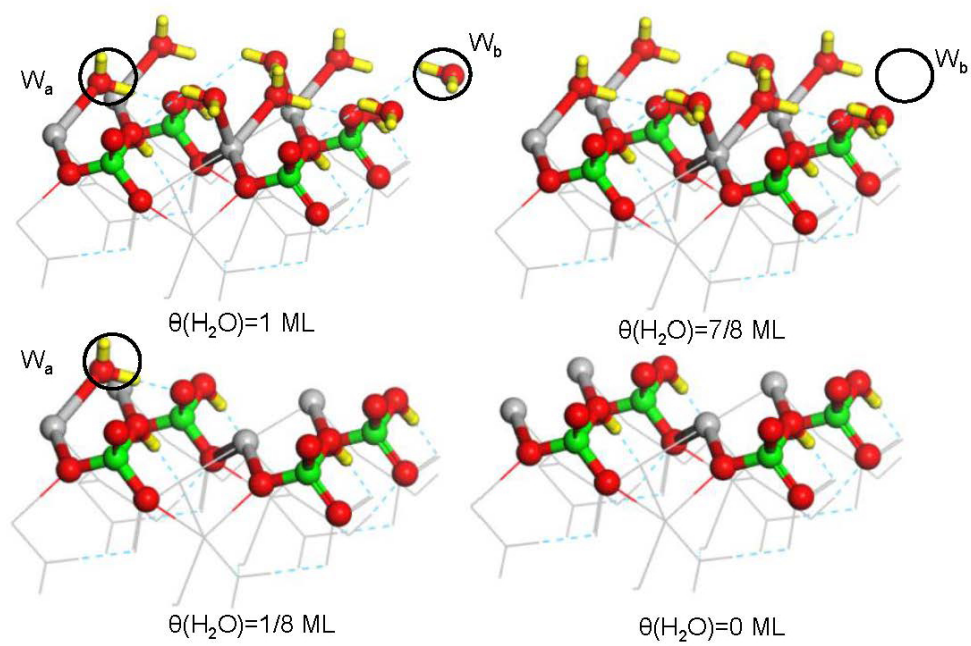


Figure 3

199x132mm (142 x 142 DPI)

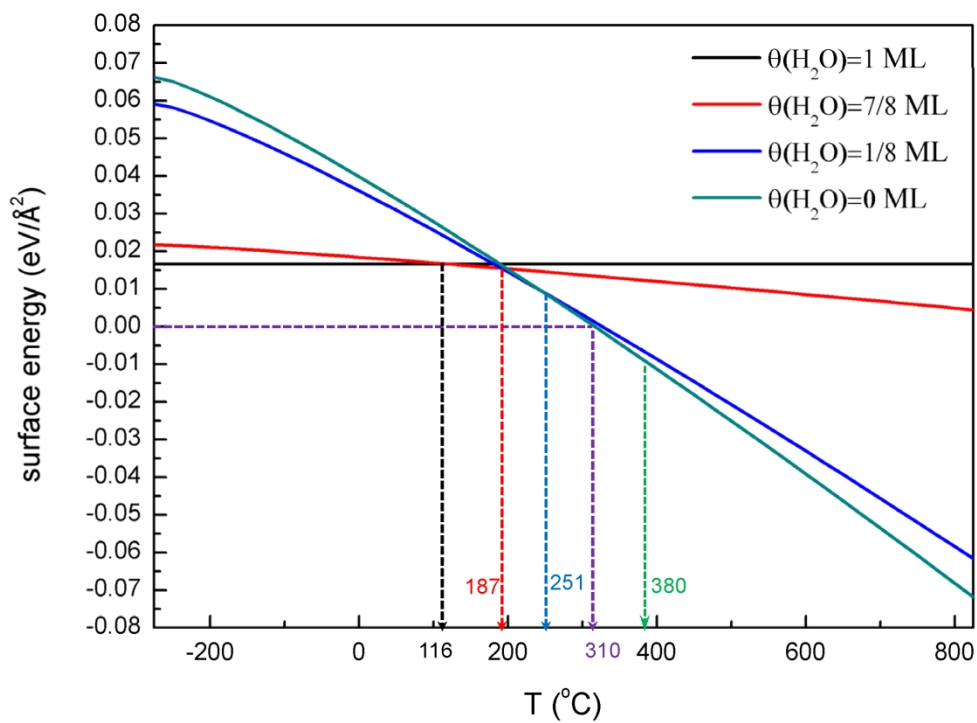


Figure4

226x165mm (300 x 300 DPI)

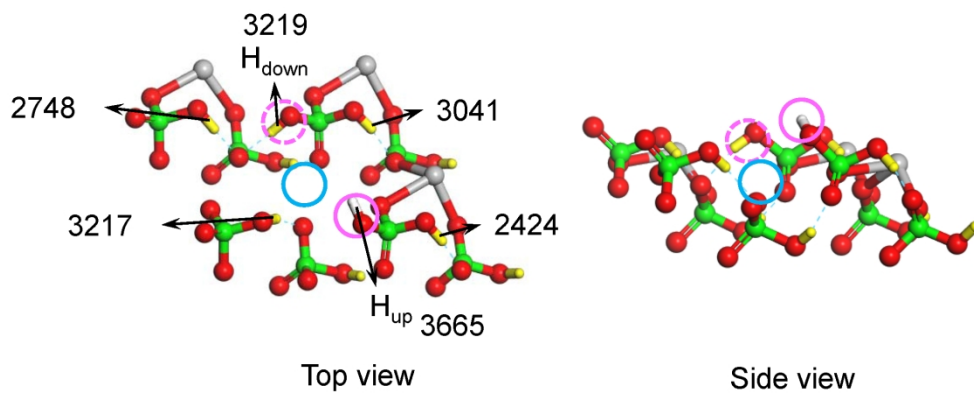


Figure 5

192x78mm (300 x 300 DPI)

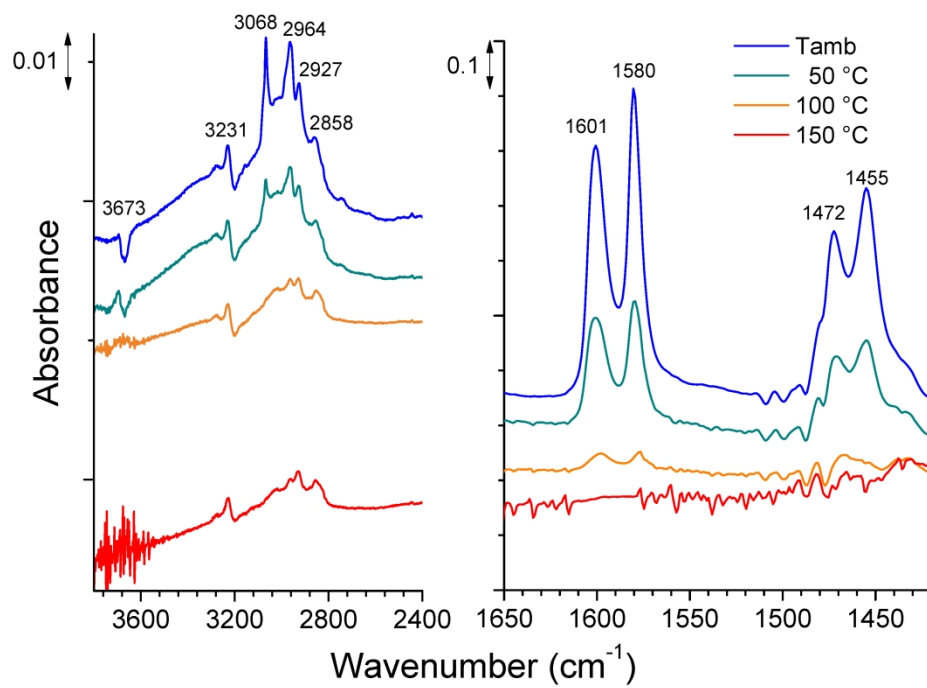


Figure6

297x210mm (300 x 300 DPI)

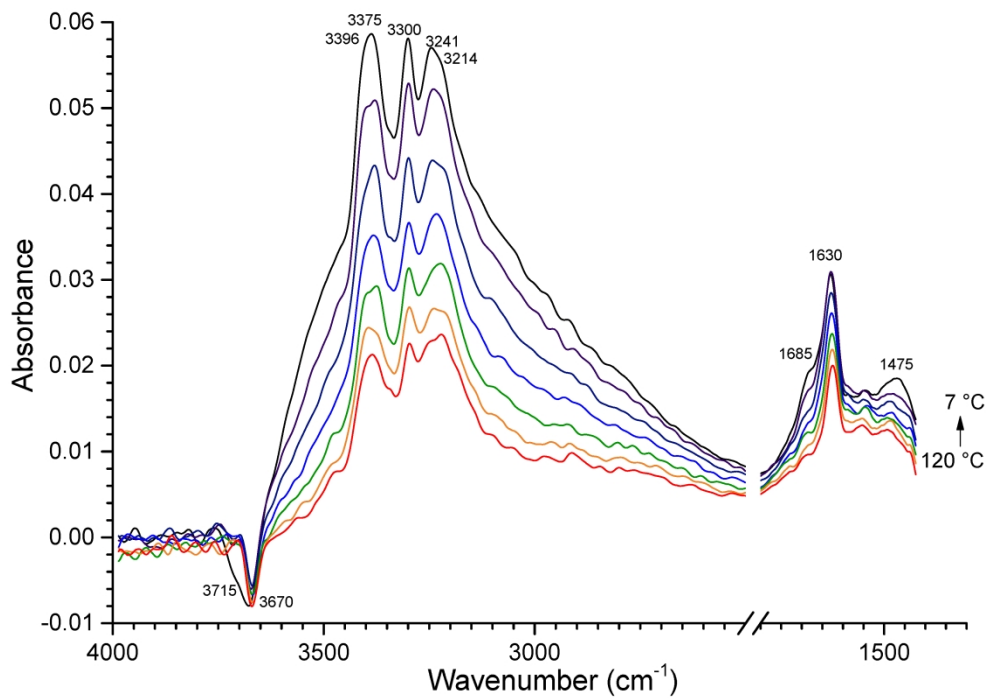


Figure7

297x210mm (300 x 300 DPI)

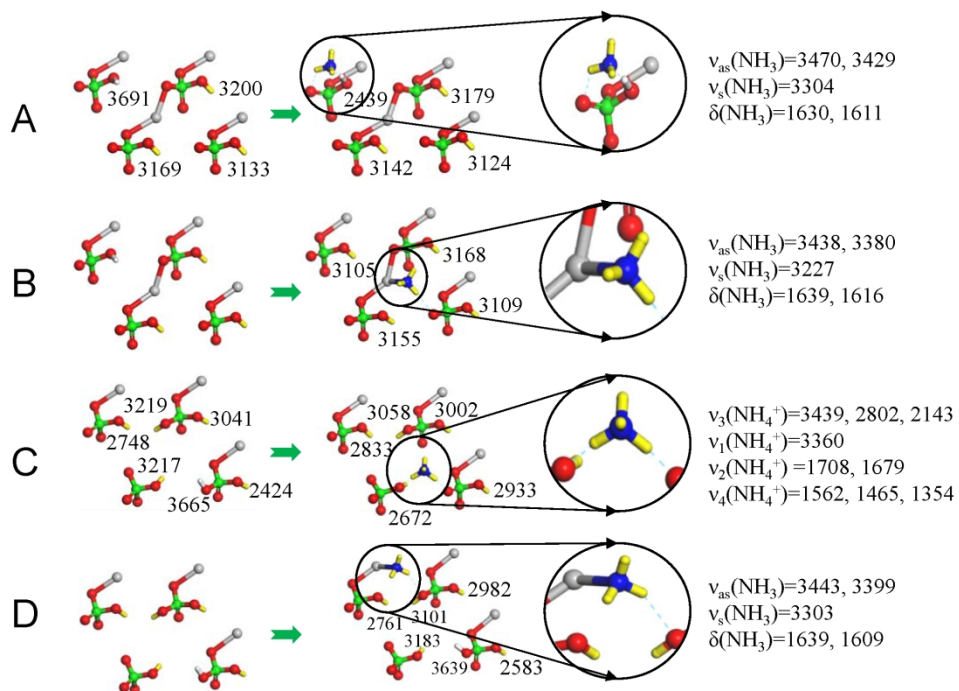


Figure8

191x135mm (300 x 300 DPI)

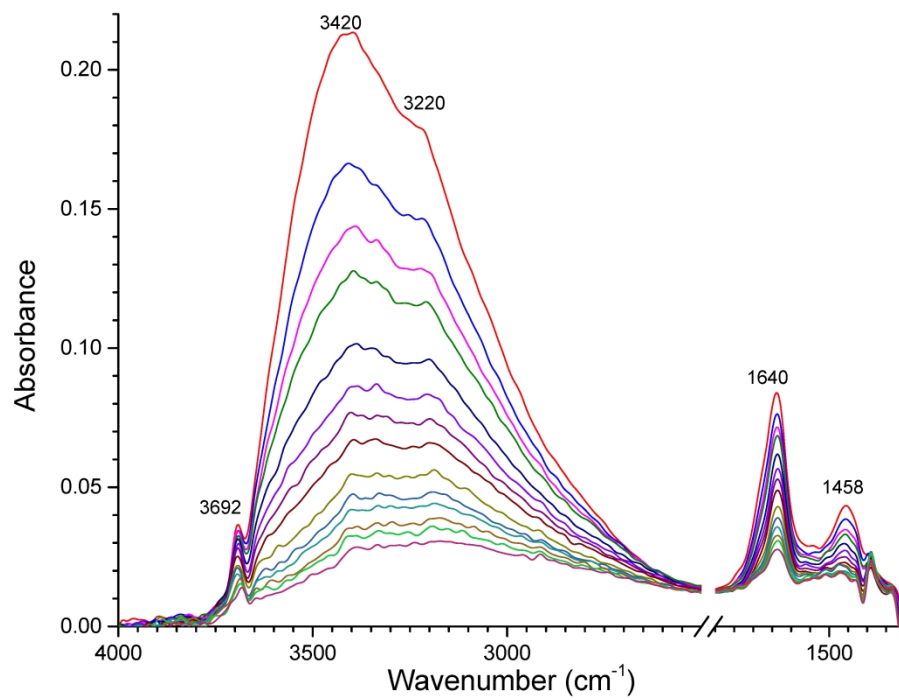


Figure9

297x210mm (300 x 300 DPI)

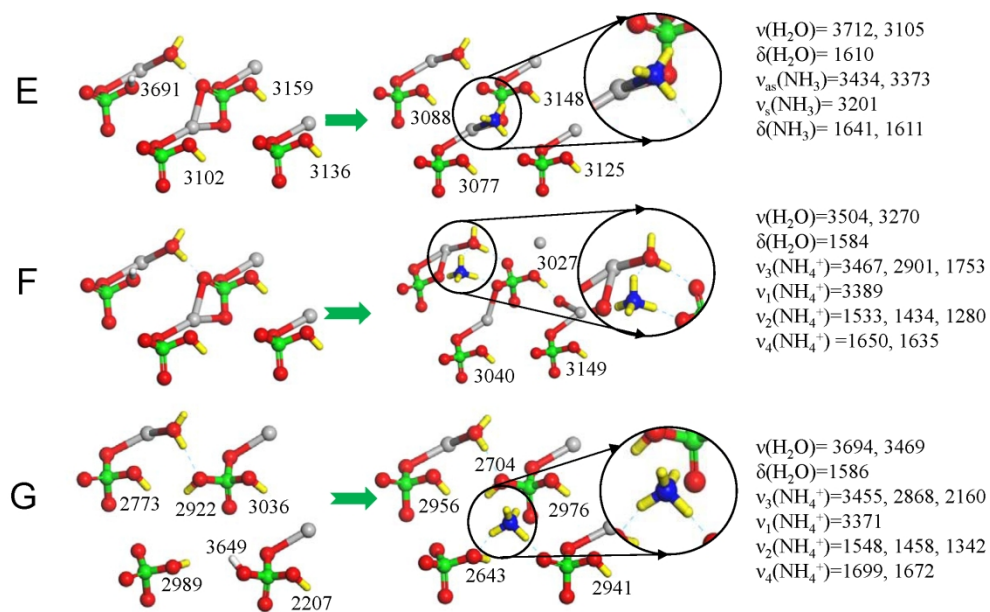


Figure10

204x129mm (300 x 300 DPI)

